

1
2
3 **Evaluation of Real-time Convection-Permitting Precipitation Forecasts in China**
4 **During the 2013-14 Summer Season**

5
6
7 Kefeng Zhu¹, Ming Xue^{1,2}, Bowen Zhou¹, Kun Zhao¹, Zhengqi Sun¹, Peiling Fu¹

8
9 Yongguang Zheng³, Xiaoling Zhang³ and Qingtao Meng³

10
11 ¹*Key Laboratory of Mesoscale Severe Weather/Ministry of Education and School of*
12 *Atmospheric Sciences, Nanjing University, Nanjing, 210093, China*

13
14 ²*Center for Analysis and Prediction of Storms and School of Meteorology, University of*
15 *Oklahoma 73072, United States*

16
17 ³*National Meteorological Center, Chinese Meteorological Administration, Beijing, China*

18
19
20 Submitted to Journal of Geophysical Research

21
22 July, 2017

23 Revised October and November 2017

24
25 *Corresponding author address*

26 Ming Xue

27 School of Atmospheric Sciences, Nanjing University, Nanjing, China, 210093 and Center
28 for Analysis and Prediction of Storms, Norman Oklahoma 73072, USA

29 Email: mxue@ou.edu

30
31 **Key Points:**

- 32
- 33 • Precipitation forecasts are produced at a 4-km convection-permitting resolution over China in summer of 2013-14.
 - 34 • The 4-km forecast outperforms global forecasts in terms of spatial distribution, intensity, timing and duration of heavy precipitation.
 - 35 • The unique intra-seasonal movement, diurnal cycles, and propagation of summer precipitation in China are also well forecast.
- 36
37
38

39

40

Abstract

41 Forecasts at a 4-km convection-permitting resolution over China during the summer
42 season have been produced with the Weather Research and Forecasting (WRF) model at
43 Nanjing University since 2013. Precipitation forecasts from 2013-14 are evaluated with
44 dense rain gauge observations and compared with operational global model forecasts.
45 Overall, the 4-km forecasts show very good agreement with observations over most parts
46 of China, outperforming global forecasts in terms of spatial distribution, intensity, and
47 diurnal variation. Quantitative evaluations with the Gilbert skill score further confirm the
48 better performance of the 4-km forecasts over global forecasts for heavy precipitation,
49 especially for the thresholds of 100 and 150 mm day⁻¹. Besides bulk characteristics, the
50 representations of some unique features of summer precipitation in China under the
51 influence of the East Asian summer monsoon are further evaluated. These include the
52 northward progression and southward retreat of the main rainband through the summer
53 season, the diurnal variations of precipitation, and the meridional and zonal propagation
54 of precipitation episodes associated with background synoptic flow and the embedded
55 mesoscale convective systems. The 4-km forecast is able to faithfully reproduce most of
56 the features while over-prediction of afternoon convection near the southern China coast
57 is found to be a main deficiency that requires further investigations.

58 1. Introduction

59 The horizontal grid spacing of numerical weather prediction (NWP) models has been
60 steadily decreasing from hundreds of kilometers in the 1950s [*Bolin, 1956; Shuman,*
61 *1957*], to $O(10)$ km or less [*Sun et al., 2013*] while the number of vertical levels has
62 increased by an order of magnitude. With rapid development of computational
63 technology, national meteorological services including the National Centers for
64 Environmental Predictions (NCEP) of the United States [*Smith et al., 2008; Benjamin et*
65 *al., 2016*], Japanese Meteorological Agency (JMA) [*Saito et al., 2006*], the U.K. Met
66 Office [*Staniforth and Wood, 2008; Tang et al., 2013*], Deutscher Wetterdienst (DWD;
67 German Weather Services) [*Baldauf et al., 2011*] and Météo-France [*Seity et al., 2011*]
68 have already been operating convective-scale models with horizontal grid spacings
69 ranging from 2 to 4 km, producing forecasts at least twice daily.

70 One major advantage of NWP models with ~ 2 -4 km grid spacings is their ability to
71 permit, to some extent, explicit representation of cumulus convection (hence the name
72 convection-permitting). At coarser resolutions (~ 10 km), the representation of convection
73 relies largely on cumulus parameterization, which have deficiencies in representing
74 convective initiation and organization [*Liu et al., 2006*], propagation [*Davis et al., 2003*],
75 and diurnal cycles (Clark et al. 2009). In contrast, when convection is explicitly
76 represented on a 2-4 km grid, forecasts of the mode, intensity, and diurnal cycles
77 generally improve [*Fowle and Roebber, 2003; Clark et al., 2007; Weisman et al., 2008*].

78 Owing to large domain size and limitation of computing resources, the China
79 Meteorological Administration (CMA)'s operational regional NWP model covering full
80 continental China used a 15 km grid spacing until 2014 when the grid spacing was

81 reduced to 10 km. As part of a national research project to improve the understanding and
82 prediction of convective-scale weather of China [Xue, 2016], and to increase the
83 collaborations between the operational and research communities, a research group at
84 Nanjing University (NJU), China, started to produce experimental 48 h real-time
85 forecasts at a 4-km grid spacing over China twice daily (launched at 00 and 12 UTC) for
86 the summer seasons (from June to August) since 2013. The forecast products were sent
87 directly to the National Meteorological Center of CMA for experimental use and
88 evaluation. This study performs a systematic evaluation of precipitation forecasts of 2013
89 and 2014 when the model configurations remained unchanged.

90 The summer period is selected because it is the main precipitation season with active
91 convective systems in China [Lin and Yang, 2014]. Improvements in the summer
92 precipitation forecasts can be invaluable because heavy rainfall is the most serious form
93 of meteorological disaster in China during warm season. According to CMA's yearbook
94 of meteorological disasters [CMA, 2016], financial losses caused by flooding are
95 estimated at 120 billion CNY (~\$18 billion USD) a year.

96 Summer rainfall in most parts of China is uniquely characterized by its close
97 association with the East Asian Summer Monsoon (EASM). As part of the EASM rainfall,
98 the main precipitation belt in China experiences two abrupt northward jumps as the
99 EASM advances inland from the southern to the northern part of China from late spring
100 through summer. Accordingly, the progression of the rainy season can be divided into
101 three stages [Ding, 1992; Ding and Chan, 2005]. The first stage, known as pre-summer
102 rainy season, begins in April in south China at the onset of EASM and ends in mid-June
103 [Luo et al., 2017]. Precipitation at this stage is mostly associated with cold or quasi-

104 stationary fronts. Organized mesoscale convective systems (MCSs) such as squall lines
105 and bow echoes often form along fronts or within the warm sector. The second stage is
106 the so-called “Meiyu” season which begins around mid-June when the western Pacific
107 subtropical high (WPSH) makes its first jump northward, relocating the major rainband
108 to the mid-latitudes. This stage typically lasts for two to four weeks [*Bao et al.*, 2011].
109 During this period, the cold polar air mass from the north and the warm moisture
110 monsoon air mass from the southern oceans meet at mid-latitudes, producing a quasi-
111 stationary west-east-oriented rainband extending thousands of kilometers (often from
112 western China through Japan). Persistent precipitation can lead to extreme flooding,
113 causing billions of annual losses.

114 The third stage begins as the EASM, along with the Meiyu rainband, advances
115 further northward in middle or late July, and lasts for about one month. High impact
116 weather events in China often occur during this stage, including the August 1975 Henan
117 “75.8” torrential rainfall [*Ding*, 2015], and the July 21, 2012 Beijing “7.21” extreme
118 rainfall [*Zhu and Xue*, 2016]. Such heavy precipitation events are often associated with
119 additional synoptic and mesoscale systems such as low-pressure vortices, low-level shear
120 lines and low-pressure troughs. In some extreme cases, circulations associated with
121 typhoons over the south China sea can facilitate extreme rainfall through moisture
122 transport [*Wen et al.*, 2015]. During the third stage, south China enters its second rainy
123 season as typhoons or other tropical systems become active. In late summer and early fall,
124 the main rainband regresses toward the south as the EASM recedes.

125 Apart from the spatial distribution of rainfall and its large-scale movement in time,
126 the diurnal cycle is another fundamental characteristic of rainfall, and exhibits unique

127 features over China in summer seasons. Owing to its large areal coverage, complex
128 terrain and long coast lines, precipitation diurnal cycles in China exhibit great regional
129 diversity [Yu *et al.*, 2014]. In southwest China, especially over the Sichuan Basin (SB,
130 Fig. 1a), precipitation generally peaks at mid-night. In middle-to-eastern China and south
131 China, dual peaks in early morning and late afternoon are found. The afternoon peak is
132 directly related to local solar heating in most land areas [Dai, 2001] while sea-breeze is
133 also a contributing factor near south China coast [Yu *et al.*, 2008]. The mechanisms
134 responsible for the morning peak are more complex, involving possible factors such as
135 the eastward propagating MCSs [Bao *et al.*, 2011], mountain-plain circulations [Sun and
136 Zhang, 2012], diurnal variations of the low-level winds [Chen *et al.*, 2010], and land-sea
137 circulations [Oki and Musiak, 1994].

138 While the climatological aspects of summer rainfall over China, including the spatial
139 distributions, seasonal movement and diurnal cycles, have been documented through
140 observations [Yu *et al.*, 2007b; Zhou *et al.*, 2008] and global model simulations [Yuan *et*
141 *al.*, 2013], the performance of regional mesoscale models, especially those at convection-
142 permitting resolutions, over contiguous China has not been systematically documented in
143 those aspects. The rainfall characteristics have been used extensively to evaluate both
144 global models [Betts and Jakob, 2002; Dai, 2006; Yuan *et al.*, 2013] and regional models
145 for other regions, especially for the United States [Davis *et al.*, 2003; Berenguer *et al.*,
146 2012]. With improved resolution, the synoptic-scale features of precipitation such as the
147 overall distribution and propagation are generally well predicted [Clark *et al.*, 2007;
148 Weisman *et al.*, 2008]. However, difficulties remain in the prediction of meso- β and
149 meso- γ scale convection which can lead to heavy and often localized intense rainfall.

150 The onset time and location, and the development and evolution mechanisms of
151 convection are still not well understood and are often not well-predicted even at
152 convection-permitting resolutions [*Berenguer et al.*, 2012].

153 So far convection-permitting models, especially the WRF model, have been most
154 extensively evaluated for continental convection over the United States in their storm
155 seasons [e.g., *Browning et al.*, 2007; *Weisman et al.*, 2008; *Berenguer et al.*, 2012] where
156 the synoptic environment is often characterized as being favorable for severe storms. In
157 contrast, the summer months of China are under strong influence of EASM, and the
158 northward migrating Meiyu rainband is a unique, prominent feature. Along the Meiyu
159 front, MCS precipitation tends to dominate while in southern China more disorganized
160 convection is more frequent. Further, over the broad area of China, there are large
161 differences in the precipitation characteristics, some strongly influenced by local terrains,
162 coast lines, and other land surface inhomogeneity. The large-scale synoptic environment
163 over East Asia is also quite different from that of the United States often. For these
164 reasons, the performance of convection-permitting models is likely different, and
165 evaluating and understanding their performance and behaviors are therefore needed.

166 Therefore, in this study, we evaluate WRF 4-km forecasts against observations with
167 particular emphases on aspects including the spatial distribution, propagation and diurnal
168 cycles of forecast precipitation, as well as their intra-seasonal variations. Quantitative
169 precipitation skills are also examined. To our best knowledge, there is no similar
170 study over China, as existing studies are either limited to one or few case studies, having
171 coarser resolutions, or covering smaller areas or shorter durations.

172 Another goal of this study is to establish the credibility (as well as identify

173 deficiencies) of the season-long forecast dataset so that future studies can be performed
174 using the dataset. In addition, systematically documenting the performance of the most
175 widely used WRF model at a convection-permitting resolution in a different climate
176 regime is worthwhile in its own right.

177 The rest of this paper is organized as follows. Sections 2 and 3 respectively introduce
178 the configurations of the forecasting system, and the observation data used for
179 verification. Section 4 performs a general evaluation of the precipitation forecasts against
180 observations in reference to operational global model forecasts. Section 5 further
181 examines the monthly mean precipitation, diurnal variations and propagation
182 characteristics of forecast. Finally, a summary and conclusions are given in section 6.

183 **2. Forecast configurations**

184 **2.1. Configurations of the NJU realtime 4-km forecasting system**

185 The NJU 4-km forecasting system is based on the Advanced Research WRF model
186 [Skamarock *et al.*, 2005] Version 3.3.1 (referred to as WRF_NJU or just WRF hereafter).
187 The forecasts were produced twice daily, starting from NCEP Global Forecasting System
188 (GFS) 0000 and 1200 UTC analyses at 0.5° horizontal resolution, and forced at the lateral
189 boundaries by NCEP GFS real-time forecasts at 3-hourly intervals. The model domain
190 has 1408×1080 horizontal grid points at a 4 km grid spacing with 50 vertical levels (see
191 Fig. 1a). Key physics schemes used include the Morrison 2-moment microphysics
192 [Morrison *et al.*, 2005], the Asymmetrical Convective Model version 2 (ACM2)
193 planetary boundary layer scheme [Pleim, 2007], the Pleim-Xiu land surface and surface
194 layer schemes [Pleim, 2006], and the CAM short- and long-wave radiation schemes
195 [Collins *et al.*, 2004]. These options were chosen based on extensive tests in the context

196 of multi-physics ensemble using the same model configurations with the July 21, 2012
197 Beijing“7.21” extreme rainfall event [Zhu and Xue, 2016]. The single deterministic
198 forecast used here is also a first step toward storm-scale ensemble forecasts (SSEF) [Xue
199 *et al.*, 2007], that will be able to provide additional probabilistic forecasting information.

200 **2.2. Forecasts from operational global forecast systems**

201 To demonstrate the advantages of using a convection-permitting resolution for
202 summer precipitation forecasting in China, global forecasts from several operational
203 centers are used as references. They include CMA, NCEP, JMA, and the European
204 Centre for Medium-Range Weather Forecasts (ECMWF). Their products are widely used
205 by Chinese operational forecasters to provide precipitation forecast guidance. The NCEP
206 GFS forecasts at a 0.5° horizontal resolution and 3 h intervals were obtained from the
207 NCEP official ftp site. The rest were retrieved from The Observing system Research and
208 Predictability Experiment (THORPEX) Interactive Grand Global Ensemble (TIGGE)
209 archive [Bougeault *et al.*, 2010; Swinbank *et al.*, 2016, available online at
210 <http://apps.ecmwf.int/datasets/>] at a 0.5° horizontal resolution and 6 h intervals.

211 **3. Verification metrics and observations**

212 For quantitative precipitation verification, we will use Gilbert skill score [GSS,
213 *Gandin and Murphy*, 1992] and frequency bias (FBIAS). To assess the impact of bias on
214 GSS, bias-adjusted GSS is also calculated following Hamill [1999]. Rain gauge data from
215 ~30,000 stations are used for verification. Forecast fields are interpolated to the station
216 sites for score calculations in the observation space. Performing the verification at station
217 locations avoids the dependency of the results on the verification grid used although such
218 verifications have their own issues, including the dependency of verification results on

219 the observation network. Additional issues can arise if the network has very disparate
220 density¹.

221 Specifically, the Model Evaluation Tools (MET) package developed by the
222 Development Testbed Center (DTC) [Brown *et al.*, 2009] is used to calculate
223 precipitation verification scores in the observation space. For convenience, we first
224 linearly interpolate the global forecast precipitation fields to the 4-km WRF_NJU grid
225 using a utility from the NCEP Unified Post Processor (UPP) before passing the fields (on
226 the same grid) to MET. Note here that the intermediate interpolation to the 4-km
227 WRF_NJU grid is for convenience only. Direct interpolation from the global fields to the
228 station sites yields very similar results (tested but not shown). For WRF forecasts, we
229 also re-calculate the GSS scores by bilinearly interpolating the 4 km WRF precipitation
230 to the 0.5° degree latitude-longitude grid first. These scores are also included in the score
231 figures and are labeled WRF_NJU_05. The inclusion of the WRF scores from the 0.5°
232 degree grid allows us to assess the potential impact of ‘double penalty’ associated with
233 point-to-point verification of high-resolution fields [e.g., Gilleland, 2013].

234 The rain gauge measurements used are hourly accumulation data from CMA, and the
235 majority of the ~30,000 stations are automated weather stations. Fig. 1b presents the
236 locations of these stations, which are densely distributed in the east and sparsely in the
237 west. The mean separation distance between two adjacent stations in the eastern
238 provinces is about 7 to 8 km. Quality control procedures including removal of duplicate

¹ We note here that the interpolation from the 4 km grid of forecast precipitation fields to the station sites can be considered an observation sampling process, which effectively filters scales not representable by the observational network. This sampling process is analogous to the actual collection of observations where the observation network samples the continuous precipitation fields. Given the finite resolution of the observational network, aliasing of small scale structures to resolvable structures can and do occur.

239 sites, time and space continuity check, and exclusion of abnormal values are performed
240 (e.g., sites far away from the coast reporting more than 1000 mm day⁻¹ are discarded).
241 The data may still have some quality issues at a few sites, but such issues are limited and
242 should not affect the general results in this paper.

243 To separate the difference in the GSSs due to precipitation forecast bias, Hamill
244 [1999] computed bias-adjusted GSS by adjusting the precipitation threshold of one
245 model's forecast so that its bias is similar to that of a control forecast. In Hamill's paper,
246 the control forecast's bias happened to be close to 1. Here, we choose to use observations
247 as the reference for bias adjustment; i.e., the thresholds for individual models are adjusted
248 so that their biases are all 1. The bias-adjusted GSSs are calculated from a sum of daily
249 contingency tables. Here, the statistical significance of GSS is determined by using
250 bootstrap resampling with 3000 randomly selected times [Candille *et al.*, 2007; Pan *et al.*,
251 2014]. A two-tailed 90% confidence interval from 5% to 95% is calculated.

252 For subjective evaluations of precipitation in sections 4 and 5, the forecast and
253 observation pairs at observation sites are reanalyzed back to the 4-km WRF grid using a
254 distance-based weighting function with a 24 km influence radius. This way, comparison
255 is only made at locations where there are rain gauge observations. Choosing the
256 verification in the observation space avoids, to some extent, the issue of mismatches
257 between the observation and model resolutions (see also earlier footnote 1). For the
258 precipitation propagation and diurnal cycle comparisons in section 5, the forecast and
259 observation pairs are reanalyzed to a 0.1° degree grid (roughly the mean spacing of the
260 rain gauge stations) using Cressman scheme with a influence radius of 0.2°. Due to the
261 latitudinal or longitudinal averaging and/or monthly averaging for the Hovmöller

262 diagrams, very small scale structures are likely filtered out anyway so the smoothing
263 effects associated with the Cressman analysis should be minimal.

264 **4. Verification of precipitation forecasts in comparison to global forecasts**

265 In summer, persistent heavy rainfall tends to pose the most severe threat in China by
266 causing flooding. In this section, the WRF_NJU precipitation forecasts at 24 h and 6 h
267 accumulation periods are verified against observations, and compared to several
268 operational global forecasts. Shorter accumulation periods are not available in TIGGE
269 datasets, and are therefore not compared. All forecasts evaluated begin at 12 UTC. For
270 spatial distribution figures, forecast period from 12 to 36 h is used to avoid the initial
271 spin-up issue.

272 **4.1. 24 h accumulated rainfall**

273 Fig. 2 2a presents observed daily mean precipitation from June through August of
274 2013 and 2014. The most pronounced feature in the observations is a rainband along the
275 southeast coast that extends from Guangxi to Zhejiang Province (see Fig. 1a). Such a
276 pronounced precipitation maximum [Zheng *et al.*, 2016] along the coastline is believed to
277 be forced by convergent onshore flows due to differential friction between the ocean and
278 land [Chen *et al.*, 2014; Chen *et al.*, 2015]. Somewhat inland from the coastline in
279 northwestern Guangdong and Guangxi provinces is another region of heavy precipitation,
280 which is associated with orographic lifting by the east-west oriented Nanling Mountain
281 range [Chen *et al.* [2015]. Further west along the southern border of China in Yunnan
282 Province is another line of heavy precipitation that coincides with the southern slope of
283 the Yunnan-Guizhou Plateau (YGP, see Fig. 1a). Orographic lifting of the southerly
284 monsoon flow is mostly responsible for the rainfall in this region. In the central part of

285 China, a southwest-northeast-oriented rainband is found along the eastern slope of the
286 Tibetan Plateau (TP) and the western edge of the SB. Finally, a east-west-oriented
287 rainband due to the persistent Meiyu front is located along the middle and lower reaches
288 of the Yangtze River (YR). A clearer depiction of the Meiyu rainband is presented in
289 Figs. 8-9, and is discussed later. The overall spatial distributions of precipitation are
290 similar to those found in climatological studies based on longer-period rain gauge
291 measurements [*Zheng et al.*, 2016] and satellite data [*Huang et al.*, 2016].

292 The 4-km WRF_NJU forecasts (Fig. 2b) successfully reproduce the general patterns
293 of precipitation well, including the main regions of heavy precipitation as well as some
294 weaker patches in-between. The predicted intensity is close to the observations except for
295 the southeast coast where precipitation is over-predicted. As will be seen later, most of
296 the over-prediction occurs in the afternoon period when disorganized convection is most
297 active, especially near the southern coast where moisture is abundant. There are several
298 possible reasons for such discrepancy. First, over-prediction of convective rainfall tends
299 to occur in models using convection-permitting resolutions due to deficiencies in model
300 physics [e.g. *Schwartz et al.*, 2009; *Berenguer et al.*, 2012] and resolution. In idealized
301 squall line simulations, Bryan and Morrison [2011] found that precipitation amount does
302 not converge with resolution until a 250 m grid spacing is used. Also, heavy precipitation
303 along the southern and eastern coastlines are driven by coastal differential friction, land
304 and sea breeze circulations, and thermal and dynamic forcing of coastal mountains and
305 these processes require accurate treatment in the model. Separate studies are needed to
306 identify the true causes for the over-prediction.

307 Precipitation forecasts from global models (Figs. 2c-f) display generally similar

308 spatial patterns as the observations, although detailed features including the shape,
309 intensity, coverage and position of main precipitation regions vary among models, and
310 are less well predicted than in WRF forecasts. For ECMWF (Fig. 2c), mean daily
311 precipitation greater than 7.5 mm is predicted over a broader zone near the southern and
312 eastern coastlines. The peak values along the southern coastline are higher than those
313 observed. This is consistent with the study of Kidd et al. [2013] which found that the
314 ECMWF forecasts have wet biases on the landside of the coastal region. In addition, rain
315 intensity and coverage over southern YGP are clearly over-predicted, while the observed
316 rainband west of the SB is under-predicted. The most notable issue with the NCEP GFS
317 forecasts is that the observed precipitation band along the south and southeast coast is
318 mostly missing. Instead, disorganized heaviest precipitation is found over south China in
319 a scattered fashion. The SB rainband is mis-located further south over northern YGP. The
320 JMA forecasts reproduce the coastal rainband well, but miss the secondary rain center
321 associated with the Nanling Mountains. The heavy precipitation band to the west of SB is
322 not only mis-located to the south, but also mis-represented as a circular zone. The main
323 issue with the CMA forecast is the over-prediction of rain intensity and coverage for the
324 coastal rainband and the SB rainband. Note that the CMA model may have large intensity
325 bias in the first 2 days of the forecast but smaller bias in the following 5 days [*Swinbank*
326 *et al.*, 2016]. Overall, WRF_NJU is able to best predict the spatial distributions of heavy
327 and light precipitation among all models; being able to better resolve geographic features
328 is one of the reasons while explicit handling of convection is another.

329 To objectively evaluate the forecasts, GSSs are calculated and presented in Fig. 3.
330 For the 25 mm day⁻¹ threshold, ECMWF has the highest GSS score (see Fig. 3a). The

331 GSSs for other forecasts are comparable. The WRF_NJU forecasts do not show any
332 advantage at this threshold. For the threshold of 50 mm day⁻¹ (heavy rain), WRF performs
333 better, but not significantly better, than global models for the 0-24 h and 24-48 h
334 forecasts (see Fig. 3b). The NCEP GFS forecasts have the next highest GSSs while the
335 JMA forecasts have the lowest scores. For 12-36 h forecasts, NCEP GFS is the best. For
336 the thresholds of 100 mm day⁻¹ (very heavy rain) and 150 mm day⁻¹ (extremely heavy
337 rain), WRF forecasts are better than all global models for all forecast ranges, but only
338 significantly better than 2 or 3 global models except for the 24-48 h forecasts at the 150
339 mm day⁻¹ threshold where only the JMA forecasts are significantly worse. Note that the
340 high GSSs for CMA at 100 mm day⁻¹ apparently benefitted from its large high biases.

341 The FBIASs of forecasts are presented in Fig. 4. For the 25 mm day⁻¹ threshold, the
342 FBIAS of WRF_NJU forecasts is close to 1, indicating no bias or small bias. For higher
343 thresholds at 50 mm day⁻¹ and above (i.e., the heavy rain categories), WRF_NJU tends to
344 over-forecast with FBIAS exceeding 1 (Figs. 4b-d). The extent of over-forecasting also
345 exacerbates with increasing thresholds, approaching 1.5 and 2 for the 100 mm day⁻¹ and
346 150 mm day⁻¹ thresholds, respectively. In contrast, the global models exhibit under-
347 forecasting for nearly all thresholds (see Fig. 4), with the only exception being the CMA
348 12-36 h forecasts for the 25 mm day⁻¹ threshold. This is linked to its over-prediction of
349 precipitation area as seen in Fig. 2f. The FBIASs for global forecasts generally decrease
350 with increasing thresholds.

351 For the WRF scores discussed above, the 4-km forecasts were directly interpolated to
352 the observation sites for score calculations. In Fig. 3 and Fig. 4, WRF scores calculated
353 from forecasts interpolated the 0.5° degree grid are given as WRF_NJU_05. The GSSs

354 are actually consistently higher than those calculated from the native 4 km fields, except
355 for the 0-24 h forecasts at the 150 mm day⁻¹ threshold. Meantime, FBIASs for
356 WRF_NJU_05 are very close to 1 except for the 0-24 h forecasts at the 150 mm threshold.
357 Interpolation to the 0.5 ° degree grid acts to smooth out localized heavy precipitation,
358 thereby reducing the positive bias significantly, and the effect is clearly larger for higher
359 precipitation thresholds. With the interpolation, the precipitation fields become smoother,
360 and actually reduces the “double penalty” on high-resolution forecasts, leading to higher
361 GSSs. The GSSs of WRF_NJU_05 are higher than those of global models for all forecast
362 periods except for the lowest threshold of 25 mm day⁻¹ where ECMWF is still the best.
363 These results also suggest that the use of a high-resolution grid not only allows for the
364 resolution of more structures, but also improves the forecast of precipitation structures
365 that are resolvable by coarser-resolution grids. We have also calculated the verification
366 scores of global forecasts directly from their 0.5 degree grids (without interpolating to the
367 4 km grid first) – the scores are essentially the same (as expected). Therefore they are not
368 shown.

369 The bias-adjusted GSSs based on the idea of Hamill (1999) are presented in Fig. 5.
370 With the adjustment, WRF_NJU loses most of its advantage for the 25 and 50 mm day⁻¹
371 thresholds. For the 100 and 150 mm day⁻¹ thresholds, the GSSs of WRF_NJU remain the
372 highest among all models but the differences are no longer significant. The relatively
373 high skill of CMA at the 100 mm threshold is also much reduced. WRF_NJU_05 still has
374 higher scores than WRF_NJU for all thresholds except for 150 mm day⁻¹. The bias
375 adjustment increases GSSs overall.

376 While the bias adjustment exercise is worthwhile, doing it for forecasts with very
377 different capabilities and skills should be viewed with much caution. For a model that can
378 rarely or never forecast extreme precipitation, such a bias adjustment procedure is doing a
379 huge favor for the model. For example, the JMA model rarely forecast 150 mm day^{-1}
380 rainfall (Fig. 3), but after adjustment its GSSs are as high and in some cases even higher
381 than other models. This is achieved by reducing the thresholds to very low values. This in
382 a sense introduces a different kind of unfairness. We include the results of bias-adjusted
383 GSSs here for completeness but the results should be viewed with a serious gain of salt.
384 We note here that the global forecasts are included here mainly to provide a frame of
385 reference.

386 **4.2. 6 h accumulated rainfall**

387 Figure 6 presents the spatial distributions of observed and forecast 6 h rainfall over
388 China, time-averaged over the 2013-2014 summer seasons (note that the TIGGE data are
389 available only at 6 h intervals). As pointed out by many previous studies [Yu *et al.*, 2007b;
390 Zhou *et al.*, 2008], different regions of China show different diurnal variations. Nocturnal
391 and morning double peaks occur over most regions of China while in the SB and along
392 YR, nocturnal peak dominates [Chen *et al.*, 2009; Bao *et al.*, 2011]. For the southern
393 coastline and southern YGP, heavy precipitation bands are found in both 08~14 LST
394 (Fig. 6a) and 14~20 LST (Fig. 6b) periods. For the latter, the south China precipitation
395 band is shifted inland to the Nanling Mountains, mostly due to thermal and dynamical
396 forcing of mountains in the afternoon. For SB, precipitation first occurs on the southeast
397 slope of the basin during 20~02 LST (Fig. 6a), and some of it moves off the basin
398 northeastward with prevailing winds during 02~08 LST (Fig. 6d). The morning peak is

399 also found along YR especially in its eastern part (Fig. 6d), which is mostly related to
400 long duration Meiyu precipitation [Yu *et al.*, 2007a]. For the rest of China, afternoon peak
401 (14~20 LST) dominates, as can be seen from the heavy rainband near the southern and
402 eastern coasts and relatively (compared with other periods of the day) strong rainfall over
403 northeast China.

404 Many aspects of the 6 h WRF precipitation forecasts shown in the second row of Fig.
405 6 bear great resemblance to their observed counterparts. They include the width, length,
406 distribution as well as the precipitation diurnal variations and propagation. The latter
407 includes the northeastward propagation of the SB rain band from 20~02 LST (Fig. 6g) to
408 02~08 LST (Fig. 6h). The biggest issue is the significant over-prediction of afternoon
409 rainfall in south China (Fig. 6f) while nocturnal precipitation is much better forecast.
410 Therefore the over-prediction of 24 h rainfall by WRF_NJU (Fig. 2b) in this region is
411 mostly due to over-prediction of afternoon convective rainfall. Finally, we note that the
412 strong afternoon precipitation maximum over the northern part of the Hainan Island (Fig.
413 6b) is very well reproduced (Fig. 6f) and this maximum is strongly influenced by sea
414 breezes, as over the Florida Peninsula [Burpee and Lahiff, 1984].

415 The overall precipitation patterns from the global forecasts are similar to the
416 observations, although the detailed structures are not as well captured as in WRF_NJU.
417 The NCEP GFS forecasts produce too little rain along the southern coastline (Fig. 6i)
418 during the day, and too much rain over the Nanling Mountains and northern YGP in late
419 afternoon and early evening (Fig. 6j-k). The propagation or diurnal variations of
420 precipitation in the region are not well simulated either. Convection seems to be easily
421 triggered in GFS over northern YGP, especially in the afternoon, and in the meantime

422 shows little propagation after its formation. This is a common problem with coarse-
423 resolution models relying on cumulus parameterization [e.g., *Clark et al.*, 2009]. In the
424 ECMWF forecasts, over-prediction of rainfall over the northern slope of YGP in the
425 afternoon still exists and covers a broader area than observations (Fig. 6m-n). The
426 daytime coastal rainfall along the south and southeast coastlines are reproduced, although
427 the spatial extent appears broader than observed. In the evening, the ECMWF forecasts
428 significantly under-predict precipitation over southeast China (Fig. 6o), although the
429 nocturnal precipitation along YR is reasonably predicted (Fig. 6p).

430 The most significant issue with JMA forecasts is the overall under-prediction of
431 precipitation in all regions, except for the SB where severe over-prediction exists at night
432 (Fig. 6s-t). This result is consistent with the FBIAS analysis in section 4.1, where the
433 JMA model gives the lowest values. In the CMA forecasts, afternoon convection over
434 southern China is under-predicted. A precipitation band is predicted in western SB and
435 northern YGP from morning through midnight (08~02 LST, Fig. 6u – 5w) instead of the
436 observed peak during 02~08 LST (Fig. 6d), completely reversing the diurnal cycle of
437 precipitation in the region. In contrast, the morning-to-early afternoon precipitation
438 (08~14 LST, Fig. 6u) is significantly over-predicted in southern China in terms of both
439 coverage and magnitude, while the afternoon precipitation (14~20 LST, Fig. 6v) is under-
440 predicted. The results suggest that convection in the morning and early afternoon is
441 triggered too early and too easily, leading to too little late afternoon convection. Overall,
442 the diurnal cycles of prediction are handled worst by the CMA global model, while 4-km
443 WRF_NJU handles the diurnal cycles, propagation and distributions of precipitation best
444 among all models examined.

445 The GSSs of the 6 h rainfall are presented in Fig. 7. For the lowest thresholds of 10
446 mm, WRF_NJU performs second best behind ECMWF except for the first 6 hours, but
447 the differences are insignificant. For thresholds of 15 mm and higher, WRF_NJU
448 performs best except for the first 6 hours at 15 mm; it performs significantly better than
449 all other models at the 25 and 50 mm thresholds most times. Compared to 24 h
450 accumulations, WRF's advantages are more clear at the 6 h intervals; this is consistent
451 with its better handling of diurnal cycles and the morning precipitation peak. In fact, the
452 GSSs do also reveal the diurnal cycles, with WRF having the highest scores in the 6-12 h
453 and 30-36 h periods, corresponding to 02-08 LST. The NCEP GSSs show delayed peaks
454 in the scores. Overall, the scores are the lowest in the 18-24 h (14 – 20 LST) period,
455 suggesting that afternoon convection is the hardest to predict.

456 **5. Further evaluation of 4-km WRF_NJU forecasts**

457 Through the verifications against observations in the previous section, the superior
458 performance of the 4-km WRF_NJU precipitation forecasts over four operational global
459 models is established. With that, this section further evaluates the 4-km forecasts with
460 respect to the monthly mean precipitation, diurnal variations and propagation
461 characteristics that are unique to summer time precipitation in China.

462 **5.1. Monthly mean precipitation spatial distributions**

463 As described in section 1, summer precipitation over China shows clearly south to
464 north and back to south movements [Ding, 1992]. Fig. 8 presents the observed and
465 forecast rainfall distributions over the three summer months in 2013 separately. Overall,
466 the spatial distribution and the inner-seasonal movements of rainbands are well forecast.

467 The observed precipitation distributions in June 2013 are characterized by two main
468 zones in Fig. 8a, one in south China and one along the middle and lower reaches of YR.
469 The first zone is associated with the pre-summer rainy season when the main
470 precipitation band hovers over south China starting from the onset of EASM in April.
471 Intense precipitation is mainly found along the southeast coastline and around the
472 Nanling Mountain range. Compared to the observations, the WRF_NJU forecasts in Fig.
473 8b capture both intense precipitation regions. However, the spatial extent and intensity of
474 the coastal rainfall is over-predicted, as was also pointed out in section 4. Later this
475 month, a northward jump of the main precipitation band at around 23 June marks the
476 beginning of the 2013 Meiyu season, creating the second precipitation zone along YR in
477 the east part of China (see Fig. 8a). The Meiyu rainband is well forecast by WRF_NJU at
478 about the right location and with a similar intensity (Fig. 8b). In addition to the Meiyu
479 rainband, the local precipitation center east of TP and west of SB is also taking shape in
480 Fig. 8a. The spatial coverage and intensity of the SB rainfall are slightly under-predicted
481 in WRF_NJU.

482 In July, the main precipitation zone moves further northward to the Yellow River
483 Valley (see Fig. 1a for its location) and extends further northeast, following the inland
484 advancement of the EASM (see Fig. 8c). In WRF_NJU forecasts, while the location of
485 the north China rainband is mostly in the right place, the intensity is reduced for the
486 northeast branch along the border of China and Korea (Fig. 8d). Meanwhile, the
487 northeast-southwest oriented precipitation band around SB becomes fully developed in
488 both observations and forecasts. The coverage of the rainband is somewhat exaggerated
489 towards the northern end in the forecasts. In the south part of China, heavy precipitation

490 continues to be found along the south coast and along the southern edge of YGP. These
491 features are reproduced well in location by WRF_NJU, although differences exist in
492 intensity and coverage south of YGP. Finally, in the central-eastern parts of China around
493 (30°N, 112°E), a local rain center is found in the observations and reproduced by the
494 forecasts. It is associated with orographic lifting of the monsoon flows by the Dabie
495 Mountains in that particular region [Wang *et al.*, 2016].

496 In August, the intensity of the northern China rainband is greatly reduced, with some
497 precipitation still remaining in the northeast (see Fig. 8e) and captured in the forecasts
498 (Fig. 8f). Extremely heavy rainfall covers a substantial area over south China, mostly as a
499 result of several landfalling typhoons (see more details in section 5.3). The precipitation
500 forecasts exhibit great resemblance to the observations in these regions, expect that the
501 coverage and intensity over Hainan Island are over-predicted, as documented earlier in
502 section 4.2.

503 The observed monthly mean precipitation in 2014 (Fig. 9) appears quite different
504 from that in 2013 (Fig. 8). However, upon close examination, the main precipitation
505 zones including the south coast rainband, the Meiyu rainband along YR, and the SB
506 rainband can still be identified, although their onset time, location, intensity and coverage
507 differ from those in 2013. In June 2014, the coastal precipitation is weaker, while inland
508 precipitation associated with the Nanling Mountains is stronger in south China (Fig. 9a).
509 WRF_NJU again over-predict the strength and spatial extent of coastal rainfall (Fig. 9b).
510 Advancing into the Meiyu season (25 June to 18 July), a east-west-oriented rainband
511 along YR in central and east China is the most prominent feature of July precipitation in
512 Fig. 9c. The EASM did not proceed as further north inland as it did in 2013, so that the

513 northern part of China is mostly free of heavy precipitation. The main Meiyu rainband is
514 well predicted by WRF_NJU (Fig. 9d), although the forecast rainband is slightly boarder.
515 The local rainband west of SB is also very well forecast. The August rainfall in south
516 China in 2014 is much more modest compared to 2013, at last partly because no typhoon
517 made landfall that year during this period (Fig. 9e). Again, over-prediction of convective
518 rainfall along the southeast coast is the major issue found in WRF_NJU forecasts in June
519 and August of 2014 (Fig. 9b and Fig. 9f).

520 The annual variations of monthly mean precipitation patterns found in Fig. 9 are
521 largely attributed to the positioning of the WPSH. During summer seasons, northward
522 progression and westward extension of the WPSH directly affect low-level moisture
523 transport into China [*Lau and Li, 1984; Zhou and Yu, 2005*]. Fig. 10 presents the mean
524 500 hPa geopotential height overlaid with the 850 hPa horizontal water vapor fluxes for
525 the three summer months. In 2013, the ridge of the WPSH advanced northeastward into
526 China from June onwards, reaching north of 30° N in August (Fig. 10c). In comparison,
527 the WPSH in 2014 was considerably weaker and was located further offshore. Its ridge
528 remained between 25° N and 30° N in July and August (see Fig. 10d and 8f). Related to
529 the retreat of the WPSH was the persistence of a stronger mid-latitude East-Asia trough
530 over east China. Associated with such mid-level circulations, the low-level moisture
531 transport into China was weaker in 2014 than 2013, and hence unable to penetrate deep
532 into northern China (compare Fig. 10c to 10d). This explains why heavy precipitation
533 was found over northern China (see Fig. 8b) in July 2013, while for 2014, the main
534 rainband was in the central region of China along YR (Fig. 9b). Both patterns are

535 reasonably reproduced by the WRF_NJU forecasts as described before (see Figs. 8d and
536 9d).

537 **5.2. Mean precipitation diurnal variations**

538 In this subsection, the daily precipitation variation and as well as the precipitation
539 diurnal cycle are further examined. The observed and forecast daily maximum and mean
540 precipitation of WRF and global model forecasts, averaged over all rain gauge stations,
541 for each summer day in 2013-14 are presented in Fig. 11. Overall, the WRF_NJU
542 forecasts closely follow the observations for both daily maximum and mean precipitation
543 while the global models have similar performance for mean precipitation but significantly
544 under-predict the daily maxima. Specifically, WRF_NJU predicts correct daily maximum
545 most times, although over-predictions including a few severe ones do occur from time to
546 time (Fig. 11a). This is consistent with Fig. 4, where WRF_NJU is found to over-predict
547 heavy rain events (≥ 50 mm day⁻¹) and most of these extreme amounts were actually
548 associated with landfalling typhoons. The correlations between the observed and forecast
549 time series for daily maximum precipitation are 0.66, 0.40, 0.56, 0.60 and 0.52 for
550 WRF_NJU, NCEP GFS, ECMWF, JMA and CMA, respectively, with the correlation of
551 WRF_NJU being the highest. Nevertheless, because correlation coefficient does not take
552 into account amplitude error, these numbers do not full reflect the relative quality of
553 forecasts; from Fig. 11a, it is clear that the global models seriously under-predict the
554 daily extreme rainfall, with JMA being the worse. For daily mean precipitation, all
555 forecasts perform well in terms of the correlation coefficient, given the relatively easy
556 task of getting the day-to-day trend right (Fig. 11b). The correlations are 0.90, 0.93, 0.94,

557 0.91 and 0.91 for WRF_NJU, NCEP GFS, ECMWF, JMA and CMA, respectively. In
558 terms of the amplitude, CMA has the most serious over-prediction (Fig. 11b).

559 The observed and forecast 48 h time series of hourly rainfall, spatially-averaged over
560 China and time-averaged for the two summers, are presented in Fig. 12a. Forecasts
561 starting from 12 UTC (20 LST) are used for this plot. The under-prediction during the
562 first 6 hours is due to model spin-up. Time series of the observed hourly rainfall are very
563 well simulated, except for around 21 and 45 hours of forecast or 17 LST when slight
564 over-prediction occurs. The variance of the hourly rainfall, as represented by the error
565 bars, are also properly forecast, with some over-prediction around the same late-
566 afternoon hours when mean values are also over-predicted. In terms of temporal pattern,
567 both observations and forecasts exhibit bimodal structures. The highest peak is found in
568 late afternoon at 21 and 45 hours of forecast corresponding to 17 LST. A secondary peak
569 of nearly comparable magnitude occurs in early morning (06 LST) at 10 and 34 forecast
570 hours. The predicted morning peak has a one-hour delay, to 07 LST. In comparison, the
571 NCEP GFS forecasts fail to reproduce the early morning peaks in both first and second
572 24 hours. For the main afternoon rainfall peak, the NCEP GFS also gives more severe
573 over-predictions than WRF_NJU. The afternoon precipitation also occurs 2-3 hours
574 earlier (Fig. 12b). The GFS results are consistent with Yuan et al [2013], who used the
575 Community Atmospheric Model version 5 [CAM5, Neale et al., 2010] to simulate
576 summer precipitation over China. They found that CAM5 failed to reproduce convective
577 rainfall in the morning over the western and eastern plains of China while stratiform rain
578 for both regions was well simulated.

579 Following Yuan et al [2012], color maps of the observed and predicted peak hours of
580 diurnal precipitation of both summers are presented in Fig. 13. Results are obtained by
581 first obtaining the peak hour from hourly mean precipitation time series (similar to Fig.
582 12a) at each rain gauge station. The final results are interpolated onto the 4-km model
583 grid for graphic plotting. The observed patterns in Fig. 13 are similar to those from Yuan
584 et al [2012], except that more detailed structures are revealed here due to the use of
585 denser surface observations. Detailed descriptions of the daily peak hours in different
586 regions of China and discussions on their possible causes can be found in Yu et al.
587 [2007b] and Chen et al. [2010].

588 In south China (below the black parallelograms), consistent late afternoon peaks are
589 founded in both observations and forecasts in Fig. 13a-b. Note that right along the
590 southeast coastline, a narrow strip of morning peaks is observed. This behavior is also
591 reproduced in WRF_NJU. Moving towards the mid-latitudes, the forecasts tend to over-
592 predict the area of early morning to noon peaks in regions enclosed by the black
593 parallelograms. This is evident by the presence of more greens and blues within the
594 parallelogram in Fig. 13b than those in Fig. 13a. The precipitation peaks over YGP (west
595 of black parallelograms) are characterized by mostly midnight to early morning peaks,
596 with scattered late afternoon peaks in rather limited areas (Fig. 13a). This region is
597 forecast reasonably well, except that the spatial extent of late afternoon peak (red colors)
598 is a little over-predicted. Over TP (close to 100° E), the forecasts show similar late
599 afternoon and early morning peaks while over the east slope of TP and its adjacent SB,
600 midnight to early morning peaks are correctly simulated. Further north, the majority of
601 precipitation peaks transition from morning towards late afternoon. While the general

602 transition pattern from the forecasts is similar to observations, some observed morning
603 peaks within that region, encircled by the white ellipses, are not well simulated. The
604 spatial coverage of late evening peaks (purple colors) are exaggerated in the forecasts.
605 Finally, in the north-most region of Fig. 13, late afternoon peaks dominate over most of
606 the region in both observations and forecasts.

607 **5.3. Precipitation episodes and propagation**

608 Precipitation episodes and propagation within a broad region between 22° - 42° N and
609 100° - 124° E (see red box in Fig. 1b), covering the main summer precipitation regions, are
610 examined with time-space Hovmöller diagrams [*Carbone et al.*, 2002] in Fig. 14-Fig. 15.
611 To avoid the spin-up and overlap issues, daily 12-36 hour forecasts, starting from 12
612 UTC are again used. To aid cross-referencing of the episodes, main precipitation episodes
613 are labeled A through N on the Hovmöller diagrams of observations in Fig. 14 and Fig.
614 15.

615 During the first two weeks of June 2013, or in the pre-summer rainy season, the main
616 precipitation events occur mostly south of 26° N (see episodes A and C, Fig. 14a) with the
617 rain centers located over the Nanling Mountains (see also Fig. 8a). Both episodes show
618 north to south movements over periods of about 2 days, as marked by the dashed lines in
619 Fig. 14a. As China enters the Meiyu season, the main rainband jumps to mid-latitudes
620 along YR between 20 June and 8 July. Episodes D and E in Fig. 14a-b are Meiyu frontal
621 precipitation events that also exhibit southerly propagation characteristics. After that, the
622 main rainband further jumps to $\sim 36^{\circ}$ N in northern China and stays there for a month or so,
623 producing rain episodes of F, H, I, K, and L in Fig. 14 b-c. In July and August, four
624 observed precipitation episodes (G, J, M and N) associated with landfalling typhoons are

625 found at lower latitudes close to the south coast. Usually, they show south to north
626 movements. In general, the WRF_NJU forecasts are able to reproduce the meridional
627 span, the temporal duration, and the propagation characteristics of each of the main
628 precipitation episodes. However, some differences in the intensity and position of
629 precipitation streaks do exist. For example, for episode C, the forecast rainfall is closer to
630 the coastline than that in the observations before mid-June (Fig. 14a and 14d). The same
631 location discrepancy is also seen previously in the monthly mean precipitation forecasts
632 (see Fig. 8a and 8b).

633 While meridional propagation mostly represents synoptic and large-scale system
634 movement, zonal propagation corresponds mainly to the movements of embedded MCSs.
635 Labels A-N in Fig. 15 represent the same rainfall systems as those in Fig. 14. In the
636 observations, most of the precipitation episodes propagate from west to east (see dashed
637 lines A-E in Fig. 15a,b). This is due to the prevailing steering-level westerly winds over
638 mid-latitudes during the summer. Episodes with the opposite westward propagation are
639 mostly tropical cyclones (G, J, M and N) that make landfall on the east coast of China.
640 Among them, typhoon M retains strong circulation over land. Rotation of the spiral
641 rainband gives rise to some eastward movement of precipitation. Overall, the WRF_NJU
642 forecasts perform well in replicating the width of precipitation streaks as well as the
643 propagation speed and directions. These are very clearly seen with episodes B, C, D, G,
644 H, I, M and N. However, as many previous studies [*Davis et al.*, 2003; *Berenguer et al.*,
645 2012] found, biases in intensity, onset position and duration of embedded convection are
646 still noticeable, especially in details (see convection ranging from yellow to red colors in
647 Fig. 15).

648 To further investigate the mean propagation characteristics, the average time-latitude
649 and time-longitude Hovmöller diagrams, respectively, of each of the three months
650 averaged over the two years are shown in Fig. 16 and Fig. 17. The main features of the
651 Hovmöller diagrams from observations in Fig. 16a-c are the two intense precipitation
652 periods with varying intensity across summer months. The two periods occur between
653 02~08 LST in the morning and 14~20 LST in the afternoon, corresponding to the double
654 peaks found in the time series over the entire analysis region in Fig. 12.

655 In June at the lower latitudes (Fig. 16a), the early morning and afternoon peaks are
656 clearly seen. The afternoon peak is the strongest in southern China ($\sim 24^{\circ}$ N), while the
657 early morning peak extends to $\sim 30^{\circ}$ N. The early morning precipitation (at the quasi-
658 stationary Meiyu front) shows little latitudinal propagation, while convection in the late
659 afternoon shows south to north, inland propagation. The prevailing southerly flows and
660 sea breezes may be attributed to for such propagations. In July (Fig. 16b), the afternoon
661 peak in south China is greatly enhanced, while a relatively weak morning peak is found
662 around 32° N and also north of 36° N (corresponding to the Meiyu rainband precipitation
663 in early and late July, respectively). In August, as the major rainband retreats back to the
664 south, the general diurnal pattern is similar to that of June. The afternoon peak propagates
665 deeper in land (Fig. 16c), some of which is related to typhoon precipitation.

666 The onset timing and subsequent propagation of precipitation associated with the
667 morning and afternoon periods are well represented in the WRF_NJU forecasts. This is
668 also supported by the high correlation coefficients between forecasts and observations,
669 which are 0.83, 0.75 and 0.86 for June, July and August, respectively. These values are
670 close to those given in Clark et al [2009] for 4-km forecasts produced for the late spring

671 season over the United States. However, over-prediction of the intensity of afternoon
672 rainfall in south China especially in June (Fig. 16d) and August (Fig. 16f) again stands
673 out as the major forecast deficiency of WRF_NJU.

674 In the time-longitude Hovmöller diagrams in Fig. 17, the two intense precipitation
675 periods in the morning and afternoon can also be identified. The afternoon peak occurs
676 most evidently between 116° E and 122° E for all three months, and near 100° E over TP
677 and YGP, especially in June (Fig. 17a). Agreeing with Bao et al [2011], there is little
678 east-west propagation of the afternoon peak in either observations or forecasts. Compared
679 to the observations, the afternoon peaks appear stronger in the forecasts. Unlike the
680 stationary afternoon peaks, the early morning peaks show eastward propagation west of
681 112° E. The maximum morning rainfall is found between 100° E and 103° E. This is mostly
682 contributed by the precipitation over YGP as evidenced in Fig. 13. The WRF_NJU
683 forecasts exhibit similar zonal propagation pattern as observations. The correlation
684 coefficients between forecasts and observations are 0.67, 0.57, 0.56 for June, July and
685 August, respectively. They are lower than their counterparts in Fig. 16, but are still
686 considered modest. As previously mentioned, the zonal propagation mainly reflects the
687 movement of MCSs within the precipitation streaks. Although the convection-permitting
688 model is beginning to resolve convection, its accuracy still limited by the resolution.
689 Therefore, it is not surprising that the correlations for zonal propagation are not as high as
690 those for meridional propagation, a lot of which is associated with movement of synoptic
691 systems.

692 6. Summary

693 This study describes experimental 48 h real-time forecasts at a 4-km convection-
694 permitting resolution over entire China. These forecasts were produced at the Nanjing
695 University, China, twice a day using the WRF model (called WRF_NJU here) over the
696 summer seasons starting from 2013, as part of a national research project to improve the
697 understanding and prediction of convective-scale weather of China. This study presents a
698 comprehensive evaluation of the precipitation forecasts of WRF_NJU against a dense
699 network of rain gauge observations. Furthermore, the WRF_NJU forecasts are compared
700 to four operational global models' forecasts to assess the advantages of using a
701 convection-permitting resolution for summer-time precipitation in China. Aspects
702 examined not only cover the spatial distribution, timing and duration, and intensity of
703 rainfall, but also the diurnal cycles of precipitation and the propagation characteristics,
704 which are unique to summer season rainfall over China. Main findings are summarized
705 below.

706 The mean 24 h accumulated precipitation is first examined to evaluate model
707 forecasts. The 4-km WRF_NJU forecasts quite accurately reproduce the spatial extents
708 and orientations of the main regions/bands of heavy precipitation. Those include a
709 distinct narrow zone of rainfall along the south and southeast coastline, a secondary
710 region off the south coast over the Nanling Mountains, a local region along the southern
711 edge of Yunnan-Guizhou Plateau in southwest China, a northeast-southwest oriented line
712 along the western edge of Sichuan Basin, and a west-east oriented band along the
713 Yangtze River associated with the Meiyu frontal system. Compared to the observations,
714 the main deficiency of the WRF_NJU forecasts is the over-prediction of intensity and

715 coverage of precipitation near the south and southeast coast. For the global forecasts, the
716 spatial distributions of precipitation centers are less well reproduced. For example, the
717 intensity of the rainband west of the Sichuan Basin is too weak (intense) in the ECMWF
718 (NCEP GFS) forecasts. Its linear spatial extent appears too board in the CMA forecasts,
719 and is misrepresented as a circular region in the JMA forecasts. When quantitatively
720 evaluated against observations, the WRF_NJU forecasts outperform global forecasts for
721 heavy rainfall ($\geq 50 \text{ mm day}^{-1}$) events, though not significantly better. In terms of FBIAS,
722 the WRF_NJU biases are closest to unity for the moderate and heavy rainfall categories,
723 indicating nearly unbiased forecasts. For thresholds above 100 mm day^{-1} , WRF_NJU
724 tends to over-predict while the global models unanimously under-predict rainfall.

725 Further dividing 24 h rainfall into four periods of 6 h accumulated rainfall reveals the
726 onset timing of the different heavy precipitation centers. WRF_NJU forecasts show good
727 agreement with observations, reproducing the morning and afternoon peaks along the
728 south coast, and the single early morning peak west of Sichuan Basin and along the
729 Yangtze River. The previously documented over-prediction of coastal precipitation is
730 found to occur mainly in the afternoon (14 – 20 LST) over the Nanling Mountains near
731 south China coast, suggesting that the biggest challenge of quantitative precipitation
732 forecasting is with convective precipitation. In comparison, the global models did much
733 worse in reproducing diurnal variations. ECMWF performed best while JMA model
734 showed the weakest diurnal variations. Most of the serious over-prediction of the CMA
735 model happened in the morning hours (08-14 LST).

736 Apart from the bulk characteristics, the WRF_NJU forecasts are further evaluated
737 with respect to unique features of summer precipitation in China. In the monthly mean

738 precipitation distributions, the WRF_NJU forecasts reproduce the south to north
739 migration from June to July, followed by the southward retreat of the main precipitation
740 band in August as in the observations. They also capture the large differences between
741 2013 and 2014 consistent with seasonal large-scale circulation differences..

742 The diurnal variations of precipitation are examined next. Time series of WRF_NJU
743 forecast daily maximum and mean precipitation agree well with observations, expect for
744 the over-prediction of maximum precipitation over a few days. In terms of the diurnal
745 time series of domain averaged hourly rainfall, the WRF_NJU forecasts follow closely
746 the observations, exhibiting a primary peak in late afternoon (17 LST) and a secondary
747 peak in early morning (6 LST), although the magnitude of the afternoon peak is slightly
748 over-predicted. Spatial distributions of daily peak hour show that the afternoon peak
749 dominates most of China while the mid-night peak appears in the Sichuan Basin and the
750 early morning peak is prevalent along the Yangtze River at mid-latitudes. The WRF_NJU
751 forecasts reproduce the overall patterns well, except for some exaggeration of the extent
752 of the morning peak regions.

753 Rain episodes during the summer months show mostly eastward and southward
754 propagations, but episodes of westward and northward propagations associated with
755 tropical cyclone activities are also found in the Hovmöller diagrams. Inland propagation
756 of coastal precipitation in the morning is also evident near the south coast. The
757 WRF_NJU forecasts are able to reproduce the onset timing, location, duration and
758 propagation direction of the main precipitation episodes during 2013-14. The correlation
759 coefficients of Hovmöller diagrams for latitudinal propagation between forecasts and
760 observations are 0.83, 0.75 and 0.86 for June, July and August, respectively, while those

761 for longitudinal propagation are lower at 0.67, 0.57, 0.56, respectively. Compared to
762 latitudinal propagation that is usually under the influence of large scale circulations,
763 longitudinal propagation is more difficult to predict as it mainly corresponds to the
764 propagation of individual convective systems. The most prominent issue of over-
765 predicting afternoon convective precipitation near south China coast requires further
766 investigations, as do other smaller deficiencies.

767 *Acknowledgment.* This work was primarily supported by the National 973 Fundamental
768 Research Program of China (Grant No. 2013CB430103) and the National Science
769 Foundation of China (Grant No. 41405100). The work was also supported by the
770 Foundation of China Meteorological Administration special (Grant No.
771 GYHY201506006). Comments of three anonymous reviewers helped improve our
772 manuscript. The gridded data at reduced resolution including rain gauge observations and
773 WRF forecasts are available at <https://pan.baidu.com/s/1dEBTKbv> (password: sxcd). For
774 more detailed data, please contact us via email.

775

776 **References**

- 777 Baldauf, M., A. Seifert, J. Förstner, D. Majewski, M. Raschendorfer, and T. Reinhardt
778 (2011), Operational Convective-Scale Numerical Weather Prediction with the
779 COSMO Model: Description and Sensitivities, *Mon. Wea. Rev.*, *139*(12), 3887-
780 3905.
- 781 Bao, X., F. Zhang, and J. Sun (2011), Diurnal Variations of Warm-Season Precipitation
782 East of the Tibetan Plateau over China, *Mon. Wea. Rev.*, *139*(9), 2790-2810.
- 783 Benjamin, S. G., et al. (2016), A North American Hourly Assimilation and Model
784 Forecast Cycle: The Rapid Refresh, *Mon. Wea. Rev.*, *144*(4), 1669-1694.
- 785 Berenguer, M., M. Surcel, I. Zawadzki, M. Xue, and F. Kong (2012), The diurnal cycle
786 of precipitation from continental radar mosaics and numerical weather prediction
787 models. Part II: Intercomparison between numerical models and with nowcasting,
788 *Mon. Wea. Rev.*, *140*, 2689-2705.
- 789 Betts, A. K., and C. Jakob (2002), Evaluation of the diurnal cycle of precipitation, surface
790 thermodynamics, and surface fluxes in the ECMWF model using LBA data, *Journal*
791 *of Geophysical Research: Atmospheres*, *107*(D20), LBA 12-11-LBA 12-18.
- 792 Bolin, B. (1956), An Improved Barotropic Model and some Aspects of Using the Balance
793 Equation for Three-dimensional Flow1, *Tellus*, *8*(1), 61-75.
- 794 Bougeault, P., et al. (2010), The THORPEX Interactive Grand Global Ensemble, *B Am*
795 *Meteorol Soc*, *91*(8), 1059-1072.
- 796 Brown, B. G., J. H. Gotway, R. Bullock, E. Gilleland, and D. Ahijevych (2009), The
797 Model Evaluation Tools (MET): Community tools for forecast evaluation, in *25th*

- 798 *Conf. Int. Interactive Information and Processing Systems (IIPS) for Meteorology,*
799 *Oceanography, and Hydrology*, edited, p. Paper 9A.6.
- 800 Browning, K. A., et al. (2007), The Convective Storm Initiation Project, *B Am Meteorol*
801 *Soc*, 88(12), 1939-1955.
- 802 Bryan, G. H., and H. Morrison (2011), Sensitivity of a simulated squall line to horizontal
803 resolution and parameterization of microphysics, *Mon. Wea. Rev.*, 140(1), 202-225.
- 804 Burpee, R. W., and L. N. Lahiff (1984), Area-Average Rainfall Variations on Sea-Breeze
805 Days in South Florida, *Mon. Wea. Rev.*, 112(3), 520-534.
- 806 Candille, G., C. Cote, P. L. Houtekamer, and G. Pellerin (2007), Verification of an
807 ensemble prediction system against observations, *Mon Weather Rev*, 135(7), 2688-
808 2699.
- 809 Carbone, R. E., J. D. Tuttle, D. A. Ahijevych, and S. B. Trier (2002), Inferences of
810 Predictability Associated with Warm Season Precipitation Episodes, *J. Atmos. Sci.*,
811 59(13), 2033-2056.
- 812 Chen, G., W. Sha, and T. Iwasaki (2009), Diurnal variation of precipitation over
813 southeastern China: Spatial distribution and its seasonality, *Journal of Geophysical*
814 *Research: Atmospheres*, 114(D13), D13103.
- 815 Chen, H., R. Yu, J. Li, W. Yuan, and T. Zhou (2010), Why Nocturnal Long-Duration
816 Rainfall Presents an Eastward-Delayed Diurnal Phase of Rainfall down the Yangtze
817 River Valley, *J Climate*, 23(4), 905-917.
- 818 Chen, X., K. Zhao, and M. Xue (2014), Spatial and temporal characteristics of warm
819 season convection over Pearl River Delta region, China, based on 3 years of

- 820 operational radar data, *Journal of Geophysical Research: Atmospheres*, 119(22),
821 2014JD021965.
- 822 Chen, X., K. Zhao, M. Xue, B. Zhou, X. Huang, and W. Xu (2015), Radar-observed
823 diurnal cycle and propagation of convection over the Pearl River Delta during Mei-
824 Yu season, *Journal of Geophysical Research: Atmospheres*, 120(24),
825 2015JD023872.
- 826 Clark, A. J., W. A. Gallus, and T. C. Chen (2007), Comparison of the Diurnal
827 Precipitation Cycle in Convection-Resolving and Non-Convection-Resolving
828 Mesoscale Models, *Mon. Wea. Rev.*, 135, 3456-3473.
- 829 Clark, A. J., W. A. Gallus, Jr., M. Xue, and F. Kong (2009), A comparison of
830 precipitation forecast skill between small convection-permitting and large
831 convection-parameterizing ensembles, *Wea. Forecasting*, 24, 1121-1140.
- 832 CMA (2016), Yearbook of Meteorological Disasters in China (in Chinese), *Rep.*, 2-3 pp.
- 833 Collins, W. D., et al. (2004), Description of the NCAR Community Atmosphere Model
834 (CAM 3.0). NCAR Technical Note NCAR/TN-464+STR, doi:10.5065/D63N21CH,
835 edited, p. 226, National Center for Atmospheric Research, Boulder, CO.
- 836 Dai, A. (2001), Global Precipitation and Thunderstorm Frequencies. Part II: Diurnal
837 Variations, *J. Climate*, 14(6), 1112.
- 838 Dai, A. (2006), Precipitation Characteristics in Eighteen Coupled Climate Models, *J*
839 *Climate*, 19(18), 4605-4630.
- 840 Davis, C. A., K. W. Manning, R. E. Carbone, S. B. Trier, and J. D. Tuttle (2003),
841 Coherence of Warm-Season Continental Rainfall in Numerical Weather Prediction
842 Models, *Mon. Wea. Rev.*, 131(11), 2667-2679.

- 843 Ding, Y. (1992), Summer Monsoon Rainfalls in China, *Journal of the Meteorological*
844 *Society of Japan. Ser. II*, 70(1B), 373-396.
- 845 Ding, Y. (2015), On the Study of the Unprecedented Heavy Rainfall in Henan Province
846 During 4-8 August 1975: Review and assessment (in Chinese), *Acta Meteorologica*
847 *Sinica*, 73(3), 411-424.
- 848 Ding, Y., and J. C. L. Chan (2005), The East Asian summer monsoon: an overview,
849 *Meteorol Atmos Phys*, 89(1), 117-142.
- 850 Fowle, M. A., and P. J. Roebber (2003), Short-Range (0–48 h) Numerical Prediction of
851 Convective Occurrence, Mode, and Location, *Wea. Forecasting*, 18(5), 782-794.
- 852 Gandin, L. S., and A. H. Murphy (1992), Equitable Skill Scores for Categorical
853 Forecasts, *Mon Weather Rev*, 120(2), 361-370.
- 854 Gilleland, E. (2013), Testing Competing Precipitation Forecasts Accurately and
855 Efficiently: The Spatial Prediction Comparison Test, *Mon Weather Rev*, 141(1),
856 340-355.
- 857 Hamill, T. M. (1999), Hypothesis tests for evaluating numerical precipitation forecasts,
858 *Weather Forecast*, 14(2), 155-167.
- 859 Huang, A., Y. Zhao, Y. Zhou, B. Yang, L. Zhang, X. Dong, D. Fang, and Y. Wu (2016),
860 Evaluation of multisatellite precipitation products by use of ground-based data over
861 China, *Journal of Geophysical Research: Atmospheres*, 121(18), 2016JD025456.
- 862 Kidd, C., E. Dawkins, and G. Huffman (2013), Comparison of Precipitation Derived
863 from the ECMWF Operational Forecast Model and Satellite Precipitation Datasets,
864 *Journal of Hydrometeorology*, 14(5), 1463-1482.

- 865 Lau, K.-M., and M.-T. Li (1984), The Monsoon of East Asia and its Global
866 Associations—A Survey, *B Am Meteorol Soc*, 65(2), 114-125.
- 867 Lin, J., and G. Yang (2014), Spatio-Temporal Characteristics of Rainstorm in China
868 Duing 1981-2010 (in Chinese), *Meteorological Monthly*, 40(7), 816-826.
- 869 Liu, C., M. W. Moncrieff, J. D. Tuttle, and R. E. Carbone (2006), Explicit and
870 parameterized episodes of warm-season precipitation over the continental United
871 States, *Adv Atmos Sci*, 23(1), 91-105.
- 872 Luo, Y. L., et al. (2017), The Southern China Monsoon Rainfall Experiment (Scmrex),
873 *Bull. Amer. Meteor. Soc.*, 98(5), 999-1013.
- 874 Morrison, H., J. A. Curry, and V. I. Khvorostyanov (2005), A new double-moment
875 microphysics parameterization for application in cloud and climate models. Part I:
876 Description, *J. Atmos. Sci.*, 62, 1665-1677.
- 877 Neale, R. B., et al. (2010), Description of the NCAR Community Atmosphere Model
878 (CAM 5.0). NCAR Tech. Note NCAR/TN-4861STR, edited, p. 238, National
879 Center for Atmospheric Research, Boulder, CO.
- 880 Oki, T., and K. Musiake (1994), Seasonal Change of the Diurnal Cycle of Precipitation
881 over Japan and Malaysia, *J. Appl. Meteor.*, 33(12), 1445-1463.
- 882 Pan, Y., K. Zhu, M. Xue, X. Wang, M. Hu, S. G. Benjamin, S. S. Weygandt, and J. S.
883 Whitaker (2014), A GSI-Based Coupled EnSRF–En3DVar Hybrid Data
884 Assimilation System for the Operational Rapid Refresh Model: Tests at a Reduced
885 Resolution, *Mon. Wea. Rev.*, 142(10), 3756-3780.
- 886 Pleim, J. E. (2006), A Simple, Efficient Solution of Flux–Profile Relationships in the
887 Atmospheric Surface Layer, *J. Appl. Meteor. Clim*, 45(2), 341-347.

- 888 Pleim, J. E. (2007), A Combined Local and Nonlocal Closure Model for the Atmospheric
889 Boundary Layer. Part I: Model Description and Testing, *J. Appl. Meteor. Clim.*,
890 46(9), 1383-1395.
- 891 Saito, K., et al. (2006), The operational JMA nonhydrostatic mesoscale model, *Mon.*
892 *Wea. Rev.*, 134(4), 1266-1298.
- 893 Schwartz, C., J. Kain, S. Weiss, M. Xue, D. Bright, F. Kong, K. Thomas, J. Levit, and M.
894 Coniglio (2009), Next-day convection-allowing WRF model guidance: A second
895 look at 2 vs. 4 km grid spacing, *Mon. Wea. Rev.*, 137, 3351-3372.
- 896 Seity, Y., P. Brousseau, S. Malardel, G. Hello, P. Bénard, F. Bouttier, C. Lac, and V.
897 Masson (2011), The AROME-France Convective-Scale Operational Model, *Mon.*
898 *Wea. Rev.*, 139(3), 976-991.
- 899 Shuman, F. G. (1957), Numerical Methods in Weather Prediction: I. The Balance
900 Equation, *Mon. Wea. Rev.*, 85(10), 329-332.
- 901 Skamarock, W. C., J. B. Klemp, J. Dudhia, D. O. Gill, D. M. Barker, W. Wang, and J. D.
902 Powers (2005), A Description of the Advanced Research WRF Version 2 *Rep.*, 88
903 pp, NCAR.
- 904 Smith, T. L., S. G. Benjamin, John M. Brown, S. S. Weygandt, T. Smirnova, and B.
905 Schwartz (2008), Convection forecasts from the hourly updated, 3-km High
906 Resolution Rapid Refresh (HRRR) model *Rep.*, 24th Conf. on Severe Local Storms,
907 Savannah, GA, Amer. Meteor. Soc., 11.21. pp.
- 908 Staniforth, A., and N. Wood (2008), Aspects of the dynamical core of a nonhydrostatic,
909 deep-atmosphere, unified weather and climate-prediction model, *Journal of*
910 *Computational Physics*, 227(7), 3445-3464.

- 911 Sun, J., and F. Zhang (2012), Impacts of Mountain–Plains Solenoid on Diurnal
912 Variations of Rainfalls along the Mei-Yu Front over the East China Plains, *Mon.*
913 *Wea. Rev.*, *140*(2), 379-397.
- 914 Sun, J., et al. (2013), Use of NWP for Nowcasting Convective Precipitation: Recent
915 Progress and Challenges, *Bull. Amer. Meteor. Soc.*, *95*(3), 409-426.
- 916 Swinbank, R., et al. (2016), The TIGGE Project and Its Achievements, *B Am Meteorol*
917 *Soc*, *97*(1), 49-67.
- 918 Tang, Y., H. W. Lean, and J. Bornemann (2013), The benefits of the Met Office variable
919 resolution NWP model for forecasting convection, *Meteorol Appl*, *20*(4), 417-426.
- 920 Weisman, M. L., C. Davis, W. Wang, K. W. Manning, and J. B. Klemp (2008),
921 Experiences with 0–36-h Explicit Convective Forecasts with the WRF-ARW Model,
922 *Wea. Forecasting*, *23*(3), 407-437.
- 923 Wen, Y. R., L. Xue, Y. Li, N. Wei, and A. M. Lu (2015), Interaction Between Typhoon
924 Vicente (1208) and the Western Pacific Subtropical High During the Beijing
925 Extreme Rainfall of 21 July 2012, *J. Meteor. Res.*, *29*(2), 293-304.
- 926 Xue, M. (2016), Preface to the Special Issue on the “Observation, Prediction and
927 Analysis of severe Convection of China” (OPACC) National “973” Projec, *Adv*
928 *Atmos Sci*, *33*(10), 1099-1101.
- 929 Xue, M., et al. (2007), CAPS realtime storm-scale ensemble and high-resolution forecasts
930 as part of the NOAA Hazardous Weather Testbed 2007 spring experiment, in *22nd*
931 *Conf. Wea. Anal. Forecasting/18th Conf. Num. Wea. Pred.*, edited, p. CDROM
932 3B.1, Amer. Meteor. Soc., Salt Lake City, Utah.

- 933 Yu, R., J. Li, and H. Chen (2008), Diurnal variation of surface wind over central eastern
934 China, *Clim Dynam*, *33*(7), 1089-1097.
- 935 Yu, R., Y. Xu, T. Zhou, and J. Li (2007a), Relation between rainfall duration and diurnal
936 variation in the warm season precipitation over central eastern China, *Geophys Res*
937 *Lett*, *34*(13), L13703.
- 938 Yu, R., J. Li, H. Chen, and W. Yuan (2014), Progress in Studies of the Precipitation
939 Diurnal Variation over Conitiguous China (in Chinese), *Acta Meteorologica Sinica*,
940 *72*(5), 948-968.
- 941 Yu, R., T. Zhou, A. Xiong, Y. Zhu, and J. Li (2007b), Diurnal variations of summer
942 precipitation over contiguous China, *Geophys Res Lett*, *34*(1), L01704.
- 943 Yuan, W., R. Yu, M. Zhang, W. Lin, H. Chen, and J. Li (2012), Regimes of Diurnal
944 Variation of Summer Rainfall over Subtropical East Asia, *J Climate*, *25*(9), 3307-
945 3320.
- 946 Yuan, W., R. Yu, M. Zhang, W. Lin, J. Li, and Y. Fu (2013), Diurnal Cycle of Summer
947 Precipitation over Subtropical East Asia in CAM5, *J Climate*, *26*(10), 3159-3172.
- 948 Zheng, Y., M. Xue, B. Li, J. Chen, and Z. Tao (2016), Spatial characteristics of extreme
949 rainfall over China with hourly through 24-hour accumulation periods based on
950 national-level hourly rain gauge data, *Adv Atmos Sci*, *33*(11), 1218-1232.
- 951 Zhou, T.-J., and R.-C. Yu (2005), Atmospheric water vapor transport associated with
952 typical anomalous summer rainfall patterns in China, *Journal of Geophysical*
953 *Research: Atmospheres*, *110*(D8), D08104.

954 Zhou, T., R. Yu, H. Chen, A. Dai, and Y. Pan (2008), Summer Precipitation Frequency,
955 Intensity, and Diurnal Cycle over China: A Comparison of Satellite Data with Rain
956 Gauge Observations, *J Climate*, 21(16), 3997-4010.

957 Zhu, K., and M. Xue (2016), Evaluation of WRF-based convection-permitting multi-
958 physics ensemble forecasts over China for an extreme rainfall event on 21 July 2012
959 in Beijing, *Adv Atmos Sci*, 33(11), 1240-1258.

960

961

962 **List of Figures**

963 Fig. 1. (a) The WRF_NJU forecast domain. Color shading represents terrain height at 500
964 m intervals. (b) Location of over 30,000 surface stations used in this study. The red
965 rectangle encloses the region where the diurnal cycle of precipitation is calculated.

966 Fig. 2. 24-h accumulated mean precipitation (mm) in June through August of 2013-14
967 from (a) rain gauge observations, (b) WRF_NJU forecast, (c) ECMWF, (d) NCEP GFS,
968 (e) JMA and (f) CMA

969 Fig. 3. Mean GSS scores of 24-h accumulated rainfall from June to August of 2013-14
970 for (a) 25 mm, (b) 50 mm, (c) 100 mm, and (d) 150 mm rainfall. The error bars
971 represent the two-tailed 90% confidence interval [(bottom) 5% and (top) 95%] using the
972 bootstrap distribution method.

973 Fig. 4. Mean FBias scores of 24 hour accumulated rainfall from June to August of 2013-
974 2014 for (a) 25 mm, (b) 50 mm (c) 100 mm and (d) 150 mm

975 Fig. 5. As Fig. 3 but for Bias-adjusted GSS scores

976 Fig. 6. As Fig. 2 but for the 6-h accumulated rainfall. The top row presents rain gauge
977 observations for the four time periods between 08~14 (first column), 14~20 (second
978 column), 20~02 (third column) and 02~08 LST (fourth column), The remaining rows
979 show corresponding forecasts from the WRF_NJU, NCEP GFS, ECMWF, JMA and
980 CMA models, respectively. The LST is equal to UTC plus 8 hours.

981 Fig. 8. Monthly-mean 24-h precipitation of 2013. (a), (c) and (e) are the observed
982 precipitation for June, July and August, respectively. (b), (d) and (f) are the same as (a),
983 (c) and (e) but for WRF_NJU forecast.

984 Fig. 9. As Fig. 8 but for 2014.

985 Fig. 10. Monthly-mean water vapor flux at 850 hPa and geopotential height at 500 hPa.
986 The left and right panels represent year 2013 and 2014, respectively. The top, middle and
987 bottom panels are for June, July and August.

988 Fig. 11. Daily maximum, and (b) daily mean rainfall (mm day⁻¹) from 3 June to 31
989 August of years 2013-14. The black thick lines represent observations and the red thick
990 lines represent the 12~36 hour WRF_NJU forecasts starting at 12 UTC. Other thin
991 dashed lines are corresponding global forecasts. The blue dashed lines separate data from
992 year 2013 to 2014. The correlations between observations and forecasts of daily
993 maximum are 0.66, 0.40, 0.56, 0.60 and 0.52 for WRF_NJU, NCEP GFS, ECMWF, JMA
994 and CMA, respectively, and those for daily mean rainfalls are 0.90, 0.93, 0.94, 0.90 and
995 0.91, respectively for the different models.

996 Fig. 12. 48-h time series of observed and forecast starting from 12 UTC (a) hourly
997 rainfall and (b) 3-h accumulated rainfall, averaged over all rain gauge stations for the
998 summer seasons of 2013-14. Error bars represent one standard deviation of each forecast
999 hour.

1000 Fig. 13. Local solar time (LST) corresponding to the peak diurnal precipitation in the (a)
1001 observation and (b) WRF_NJU forecasts. The white ellipses and the black parallelogram
1002 highlight regions where major differences exist between observations and forecasts.

1003 Fig. 14. Time-latitude Hovmöller diagrams of rainfall in summer 2013. Rainfall is
1004 averaged from 100°E to 124°E within strips of 0.1° latitude width. The top and bottom
1005 rows represent rain gauge observations and WRF_NJU forecasts. The columns represent
1006 June, July and August. Curves and shadings below each subfigure show the maximum

1007 and mean terrain heights, respectively. Capital letters in the top row represent individual
1008 precipitation episodes.

1009 Fig. 15. As Fig. 12 but for the time-longitude Hovmöller diagrams. Rainfall is averaged
1010 from 22oN to 42oN within strips of 0.1o longitude width.

1011 Fig. 16. Hovmöller diagrams representing the diurnal cycle of precipitation averaged
1012 zonally within strips of 0.1o latitude width between 100oE and 124oE in years 2013-14.

1013 The top and bottom rows represent rain gauge observations and WRF_NJU forecasts.

1014 The columns represent June, July and August. The time-axes of left (right) are in UTC

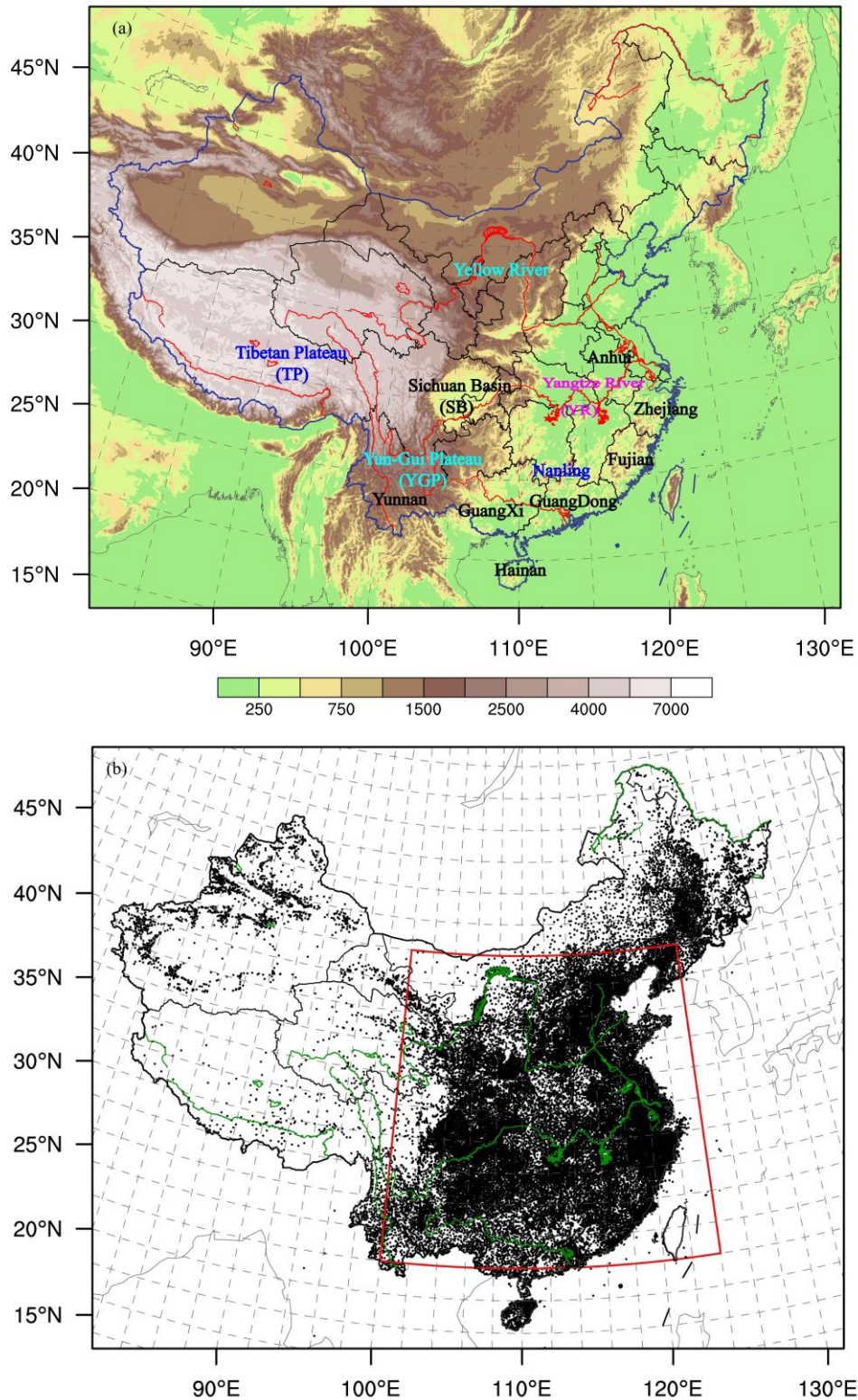
1015 (LST). Data from all 48 hours of forecast starting at 12 UTC are included. The

1016 correlation coefficient (R) of the forecast with its corresponding observation is given in

1017 the bottom panels.

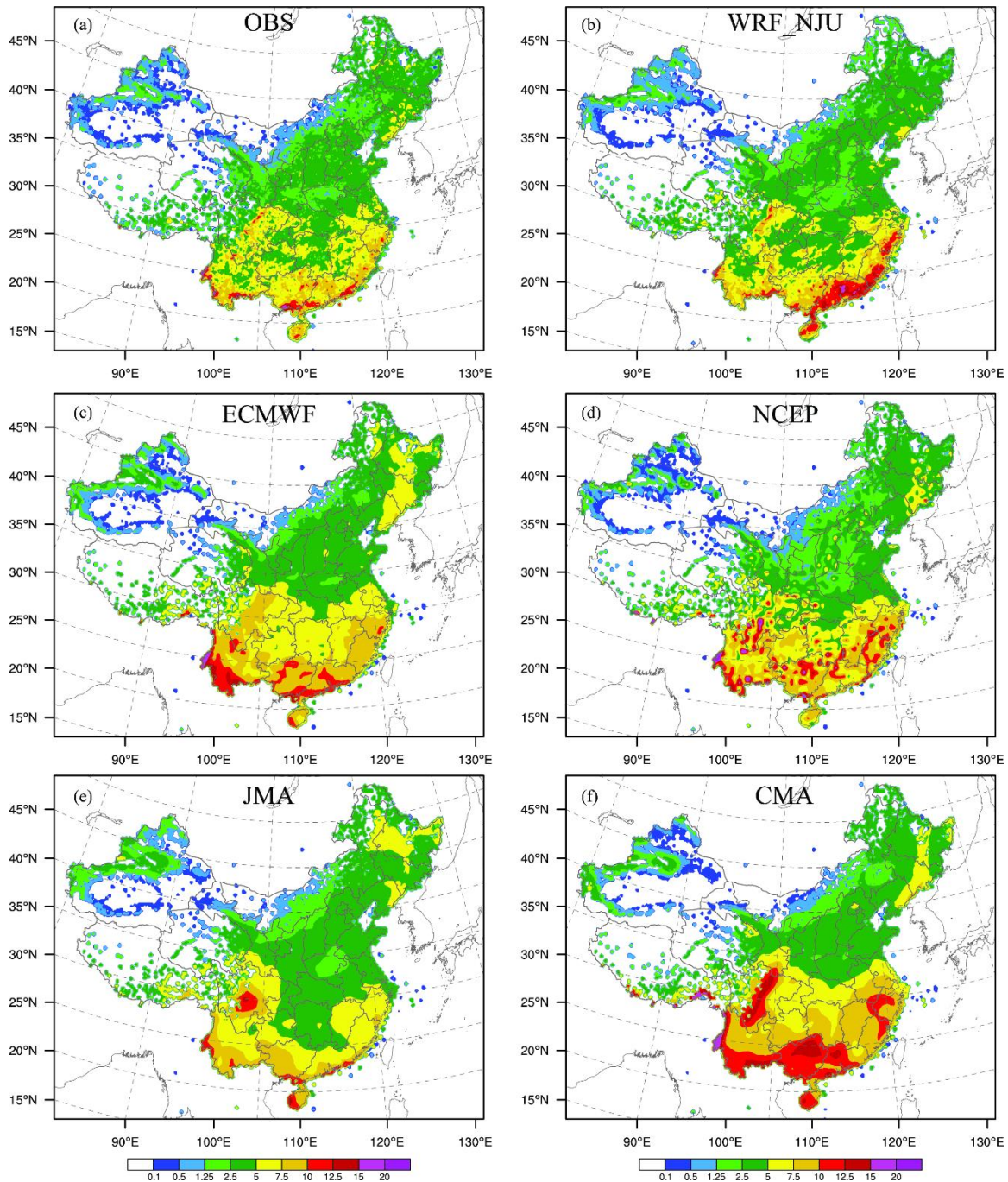
1018 Fig. 17. The same as Fig. 16 but for time-longitude diurnal cycle averaged meridionally

1019 within strips of 0.1o longitude width between 22oN and 42oN



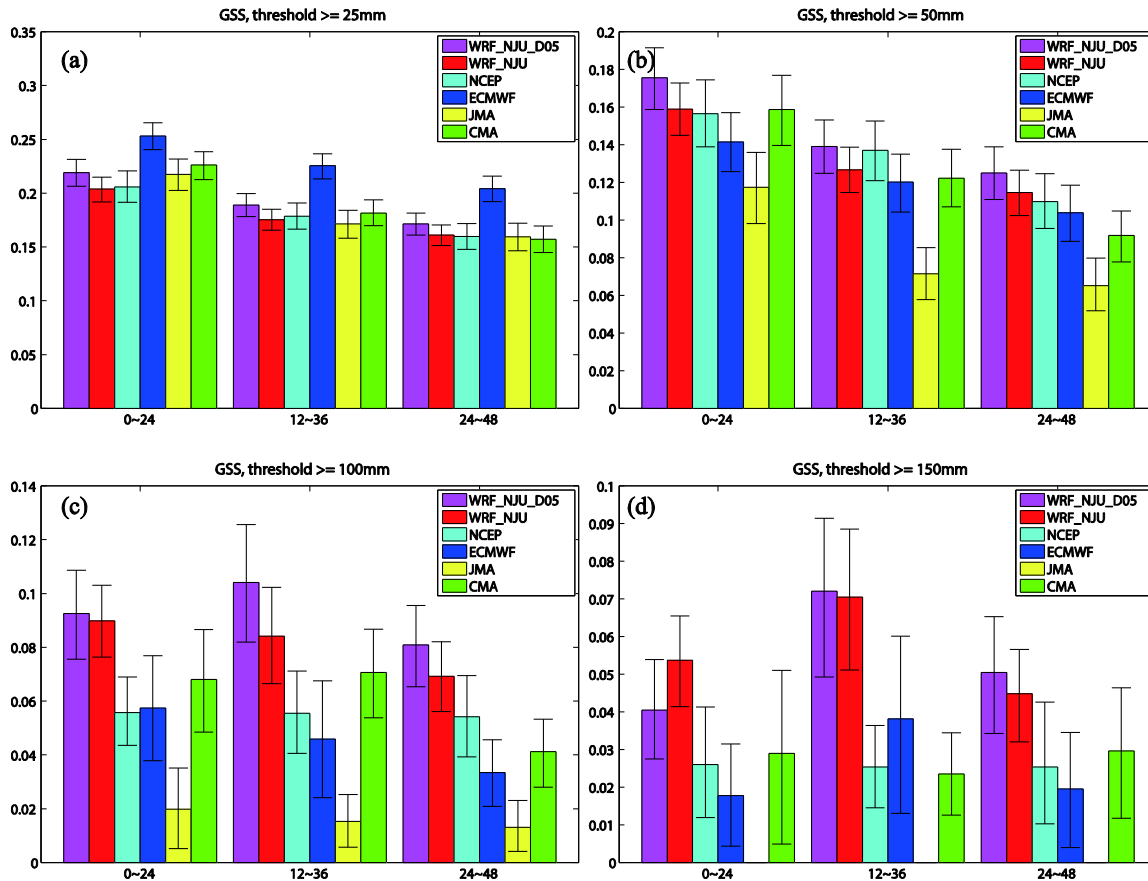
1020
 1021
 1022
 1023
 1024

Fig. 1. (a) The WRF_NJU forecast domain. Color shading represents terrain height at 500 m intervals. (b) Location of over 30,000 surface stations used in this study. The red rectangle encloses the region where the diurnal cycle of precipitation is calculated.

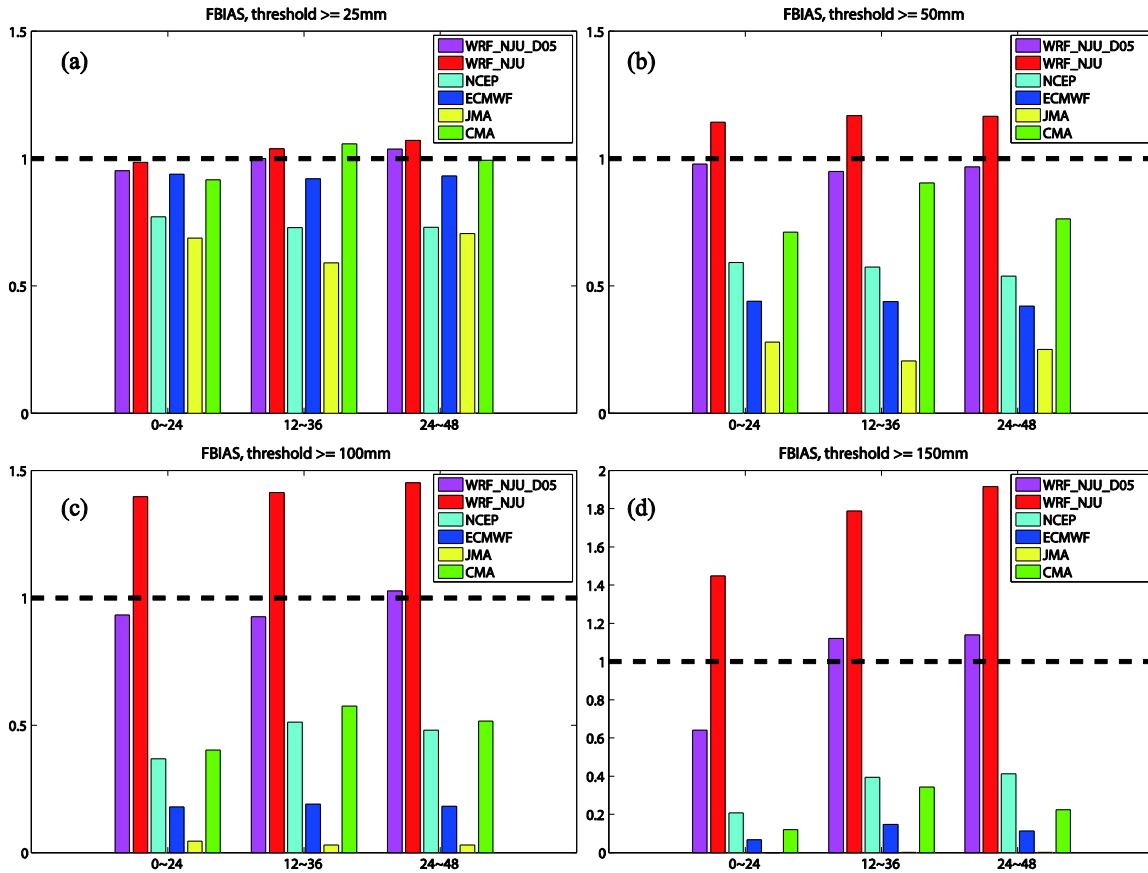


1025
 1026
 1027
 1028
 1029
 1030
 1031

Fig. 2. 24-h accumulated mean precipitation (mm) in June through August of 2013-14 from (a) rain gauge observations, (b) WRF_NJU forecast, (c) ECMWF, (d) NCEP GFS, (e) JMA and (f) CMA global forecasts. Forecasts starting from 12 UTC are used and the 24-h accumulation period is between 12 and 36 hours of forecast.

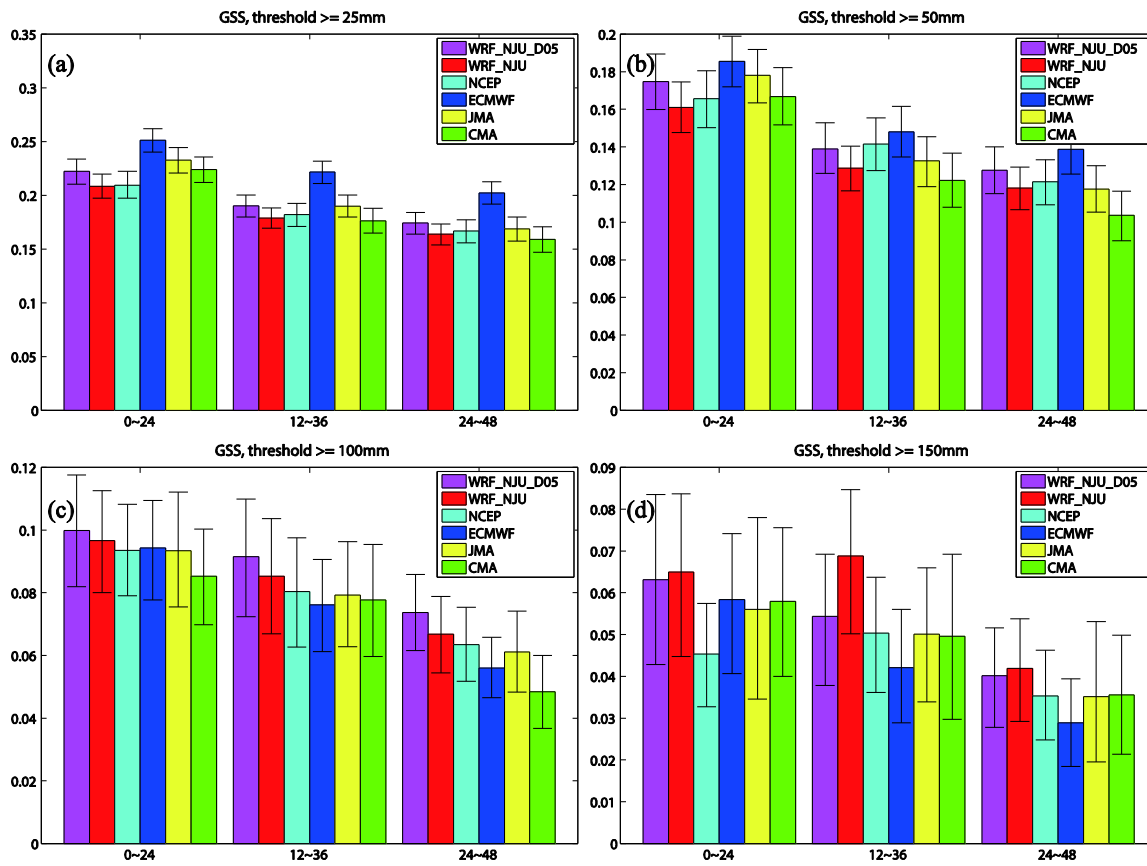
1032
1033

1034 Fig. 3. Mean GSS scores of 24-h accumulated rainfall from June to August of 2013-14
 1035 for (a) 25 mm, (b) 50 mm, (c) 100 mm, and (d) 150 mm rainfall. The error bars
 1036 represent the two-tailed 90% confidence interval [(bottom) 5% and (top) 95%] using the
 1037 bootstrap distribution method. Here, for WRF_NJU_D05, the WRF forecasts are first
 1038 interpolated to a 0.5° degree latitude and longitude grid, and then interpolated to the
 1039 observation sites for score calculations.



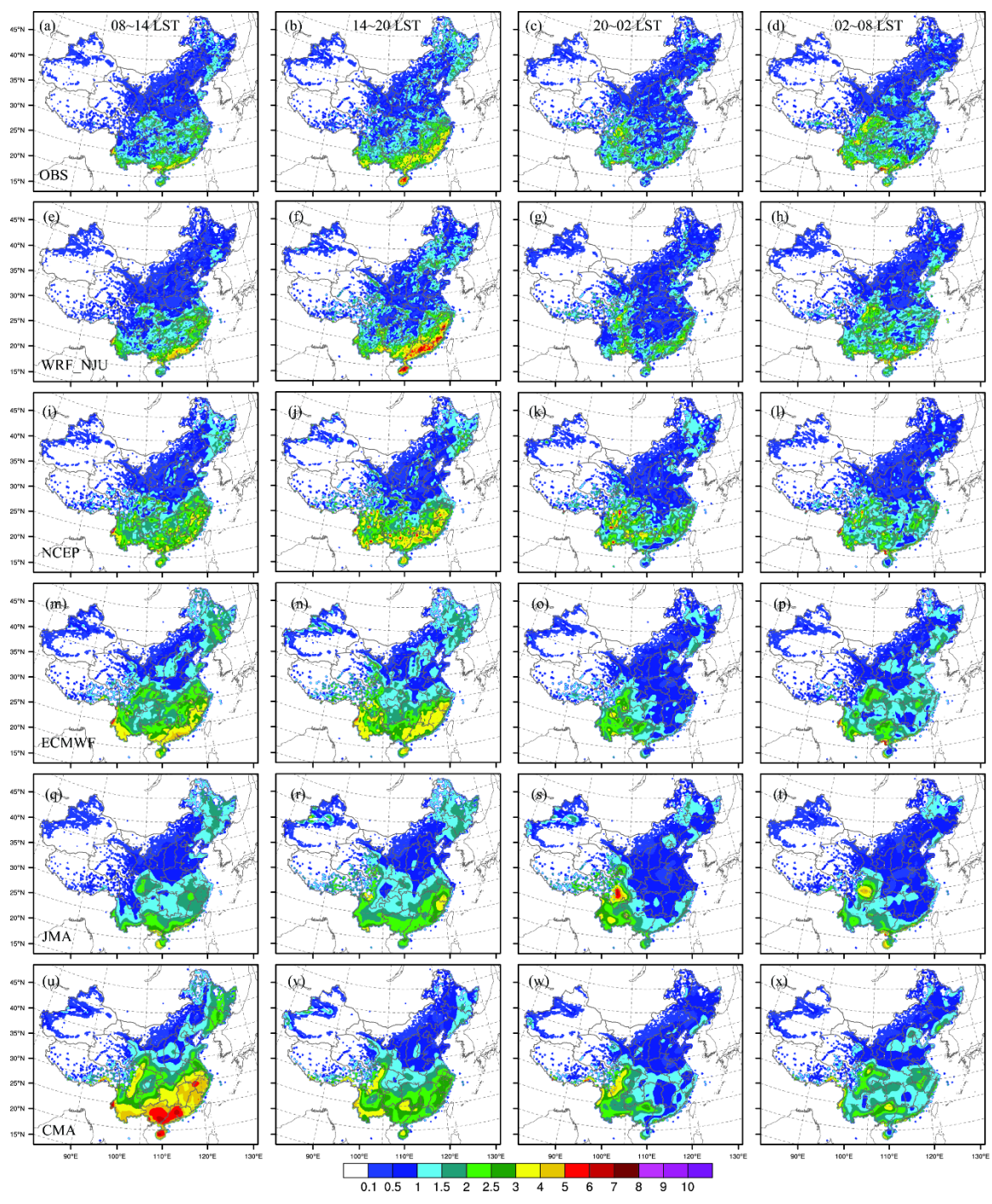
1040
1041
1042
1043

Fig. 4. Mean FBIAS scores of 24 hour accumulated rainfall from June to August of 2013-2014 for (a) 25 mm, (b) 50 mm (c) 100 mm and (d) 150 mm rainfall.



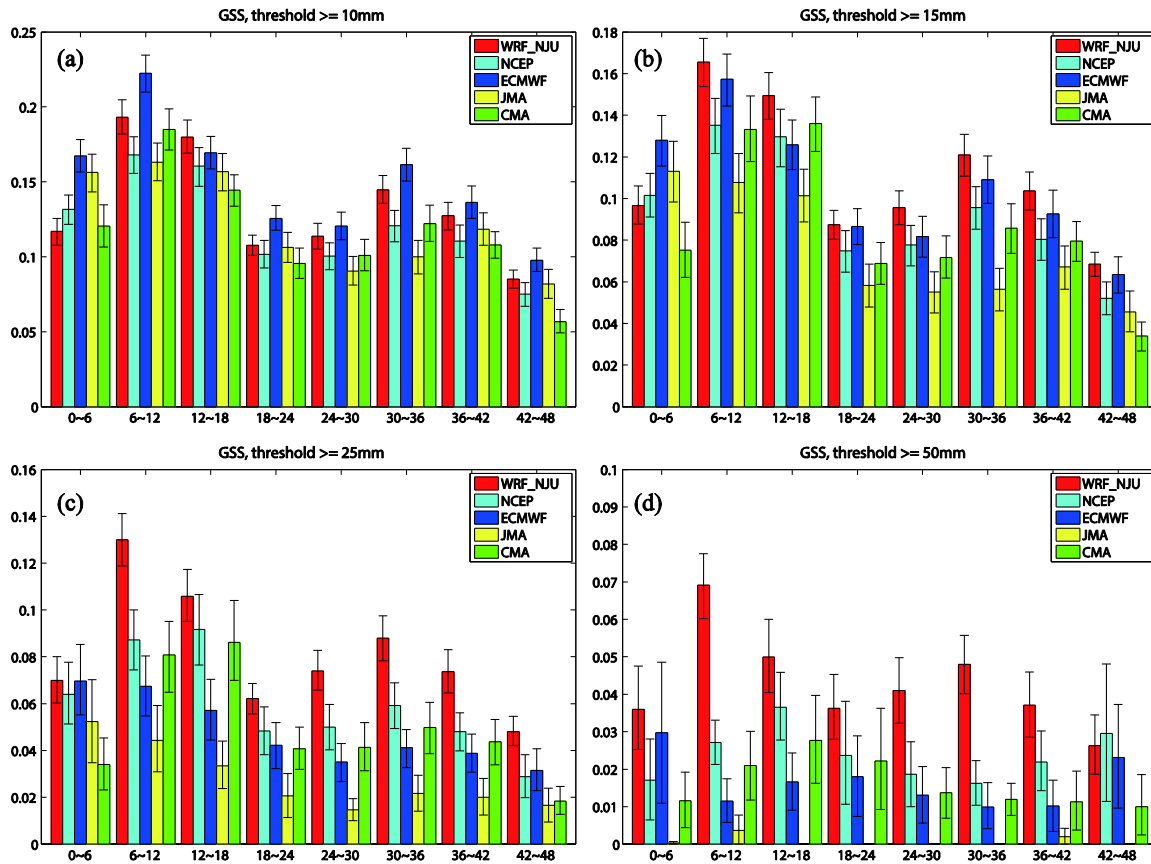
1044
 1045
 1046
 1047

Fig. 5. As Fig. 3 but for Bias-adjusted GSS scores.



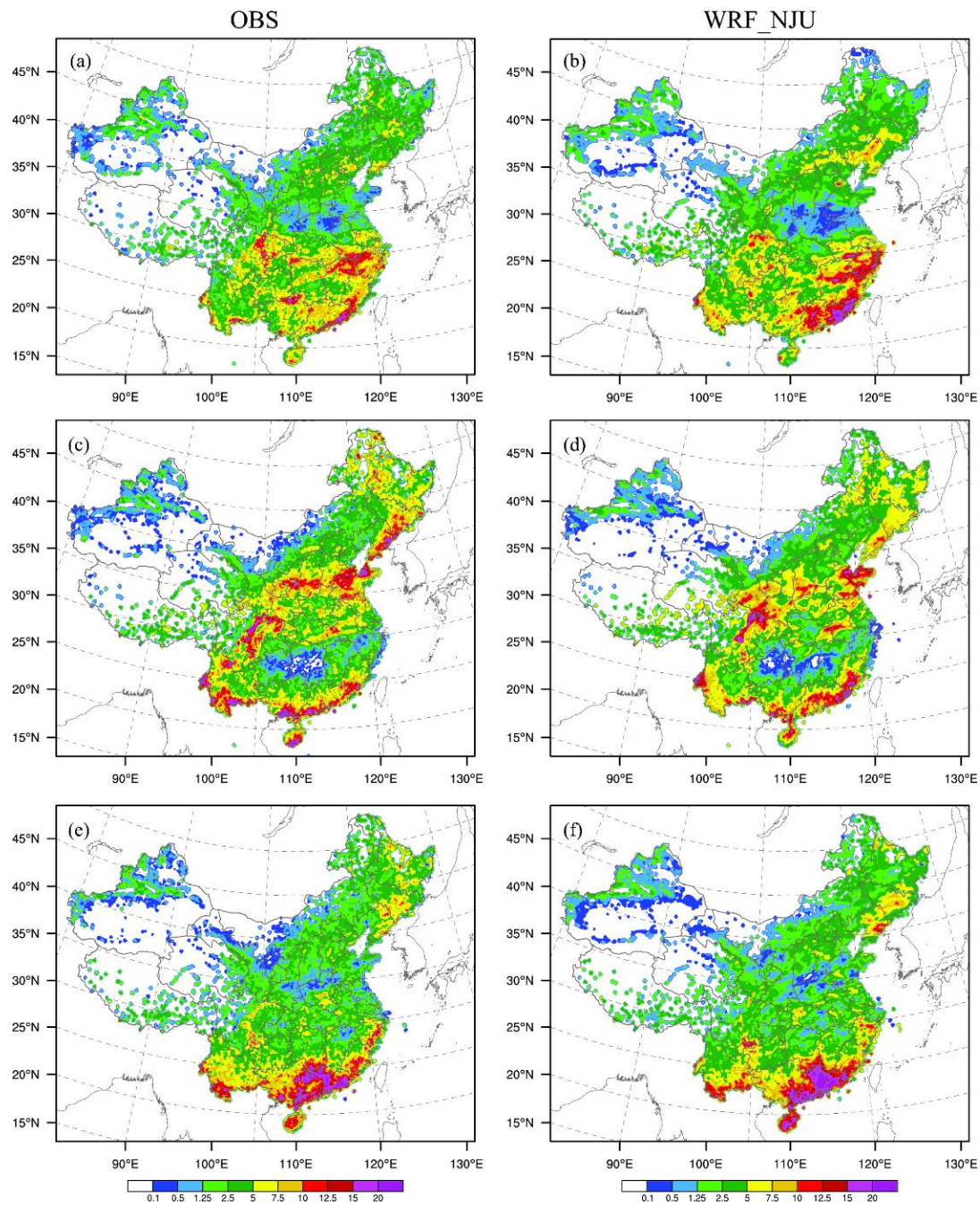
1048
1049
1050
1051
1052
1053
1054
1055
1056
1057

Fig. 6. As Fig. 2 but for the 6-h accumulated rainfall. The top row presents rain gauge observations for the four time periods between 08~14 (first column), 14~20 (second column), 20~02 (third column) and 02~08 LST (fourth column), The remaining rows show corresponding forecasts from the WRF_NJU, NCEP GFS, ECMWF, JMA and CMA models, respectively. The LST is equal to UTC plus 8 hours.



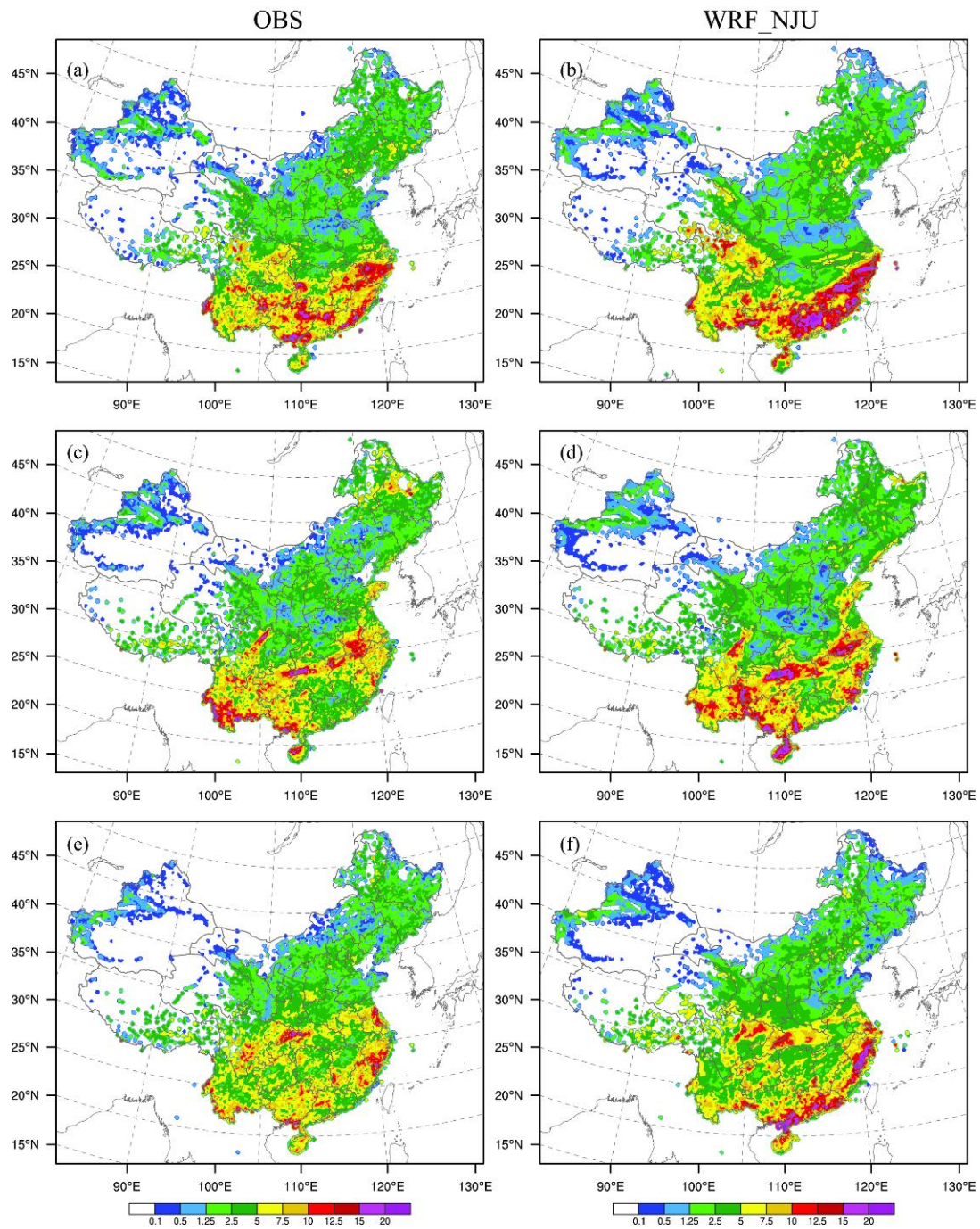
1058
1059
1060

Fig. 7. As Fig. 3 but for 6-h accumulated rainfall.



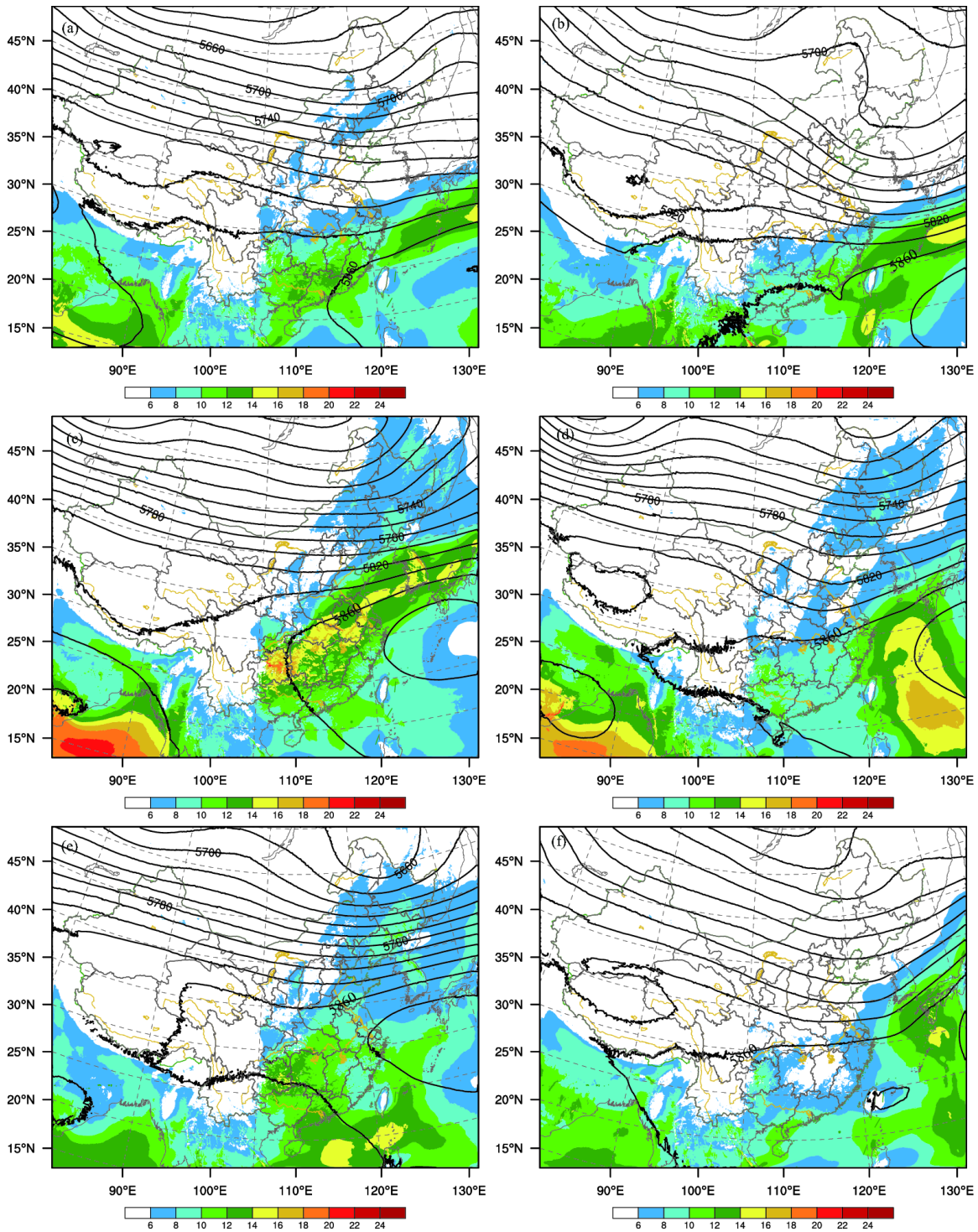
1061
1062
1063
1064
1065

Fig. 8. Monthly-mean 24-h precipitation of 2013. (a), (c) and (e) are the observed precipitation for June, July and August, respectively. (b), (d) and (f) are the same as (a), (c) and (e) but for WRF_NJU forecast.



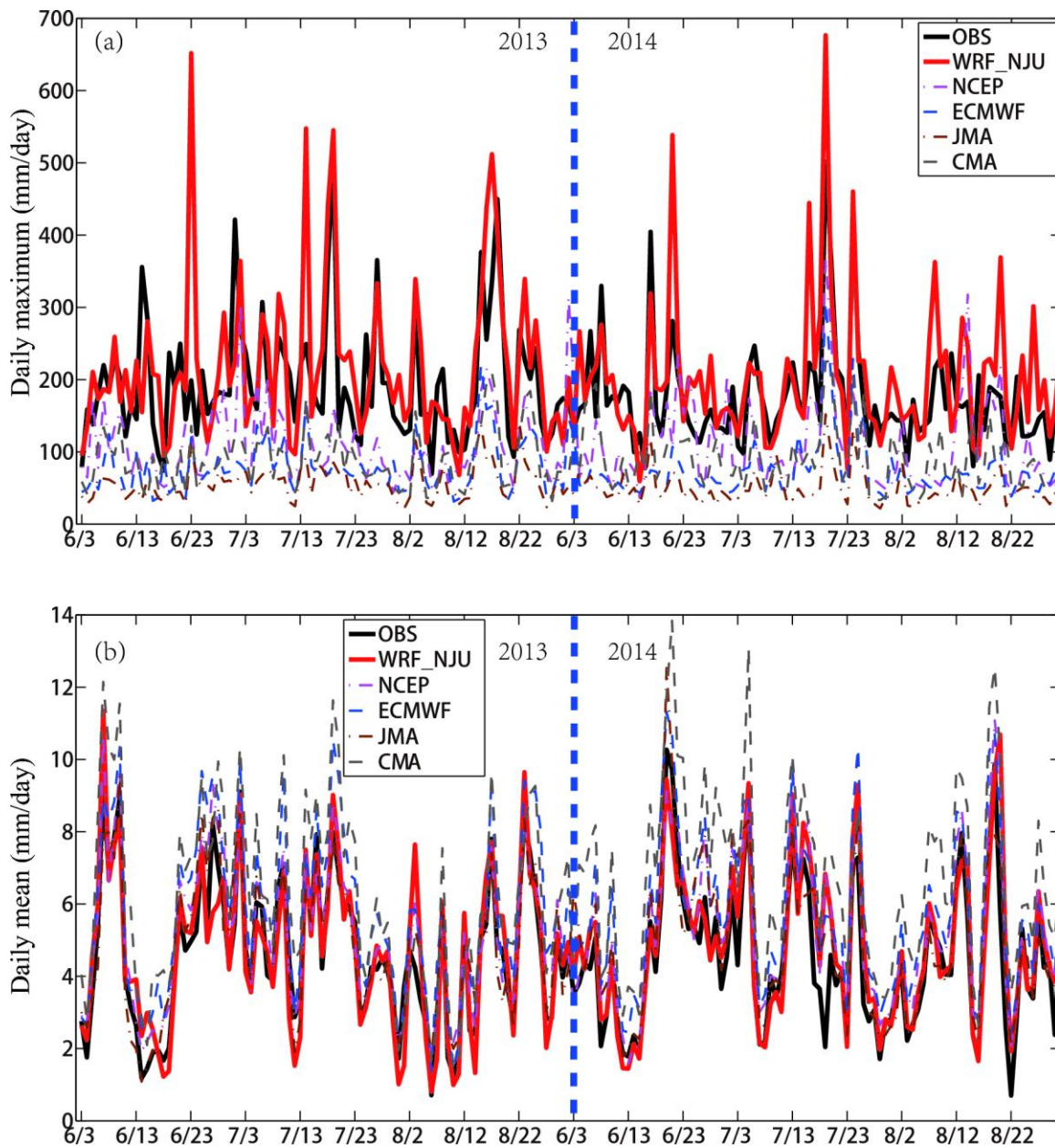
1066
1067
1068

Fig. 9. As Fig. 8 but for 2014.



1069
 1070
 1071
 1072
 1073
 1074

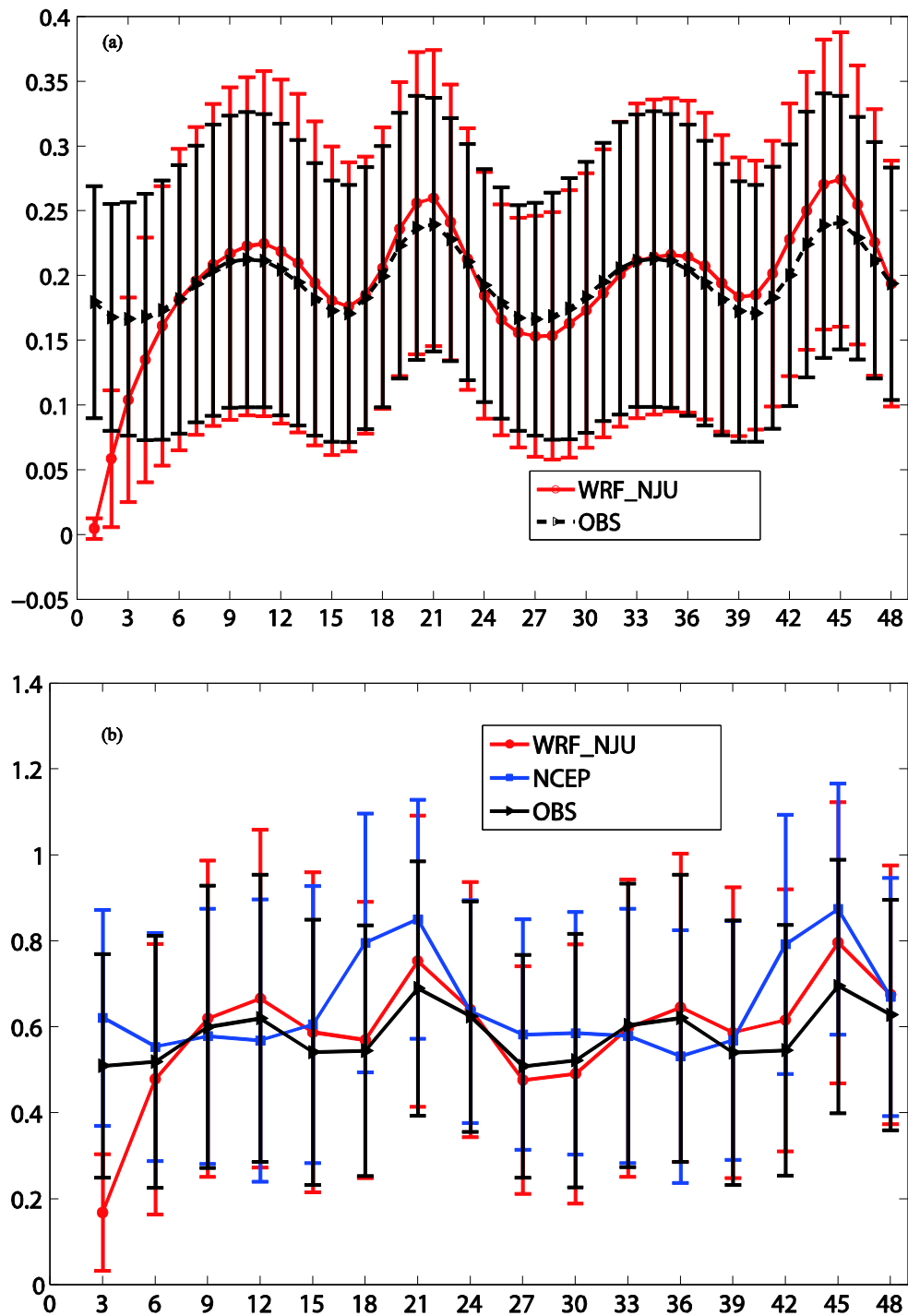
Fig. 10. Monthly-mean water vapor flux at 850 hPa and geopotential height at 500 hPa. The left and right panels represent year 2013 and 2014, respectively. The top, middle and bottom panels are for June, July and August.



1075
1076

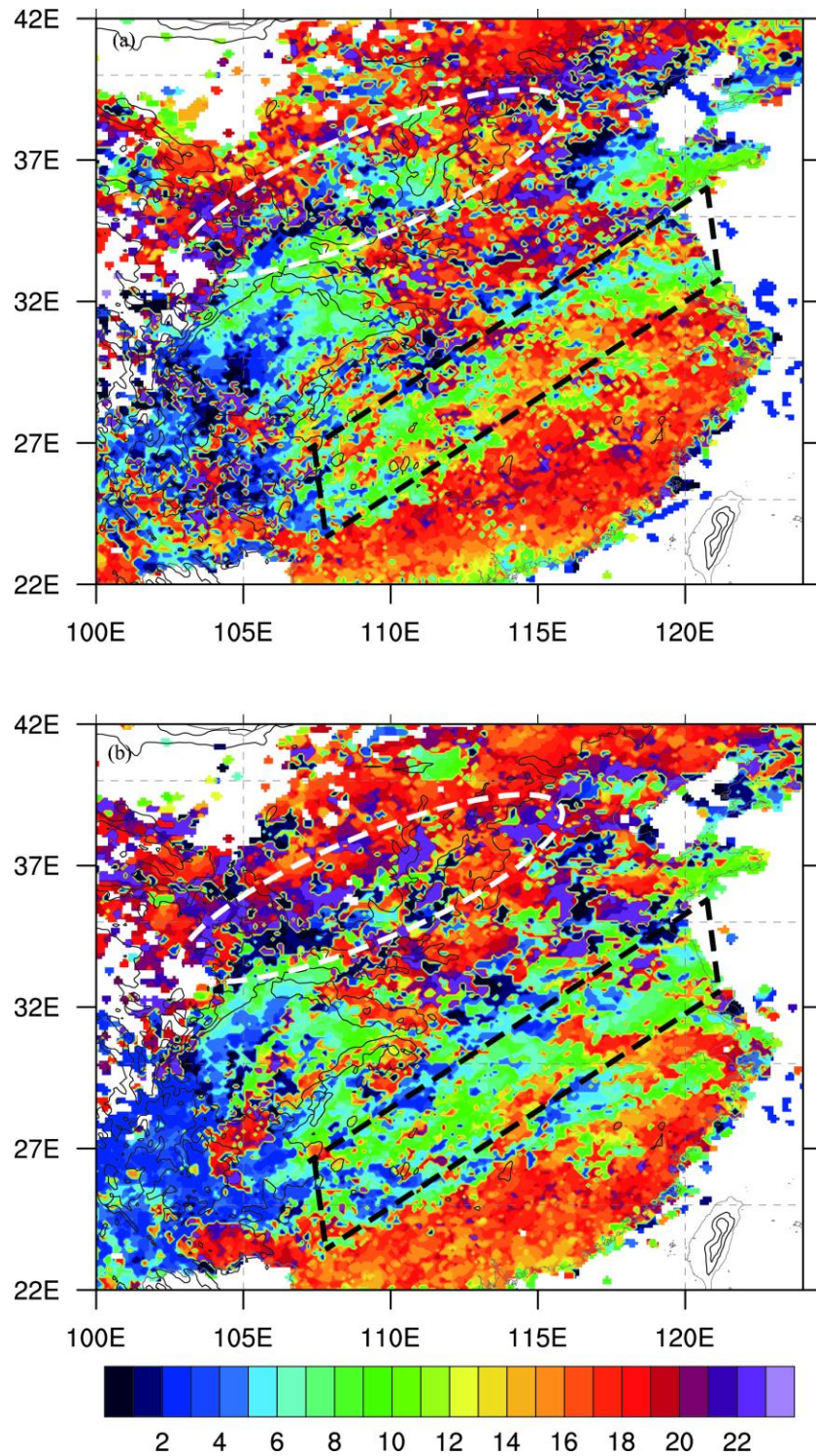
1077 Fig. 11. Daily maximum, and (b) daily mean rainfall (mm day^{-1}) from 3 June to 31
1078 August of years 2013-14. The black thick lines represent observations and the red thick
1079 lines represent the 12~36 hour WRF_NJU forecasts starting at 12 UTC. Other thin
1080 dashed lines are corresponding global forecasts. The blue dashed lines separate data from
1081 year 2013 to 2014. The correlations between observations and forecasts of daily
1082 maximum are 0.66, 0.40, 0.56, 0.60 and 0.52 for WRF_NJU, NCEP GFS, ECMWF, JMA
1083 and CMA, respectively, and those for daily mean rainfalls are 0.90, 0.93, 0.94, 0.90 and
1084 0.91, respectively for the different models.

1085



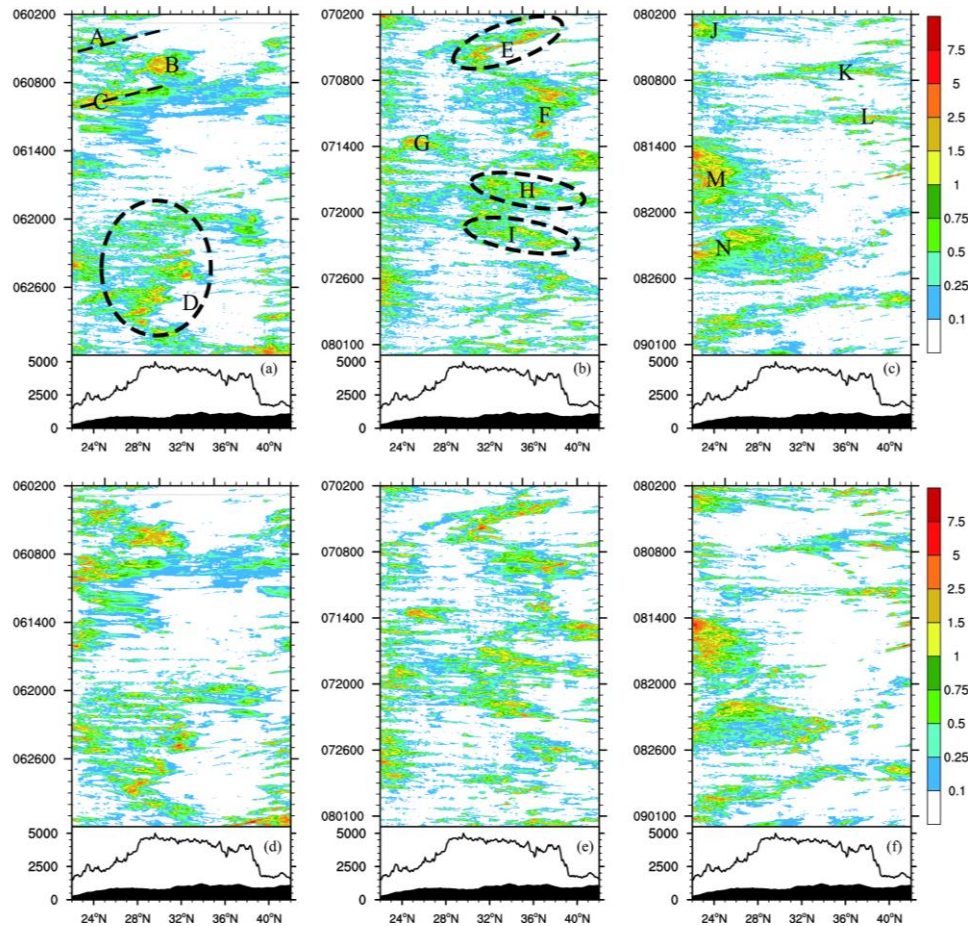
1086
1087
1088
1089
1090

Fig. 12. 48-h time series of observed and forecast starting from 12 UTC (a) hourly rainfall and (b) 3-h accumulated rainfall, averaged over all rain gauge stations for the summer seasons of 2013-14. Error bars represent one standard deviation of each forecast hour.



1091

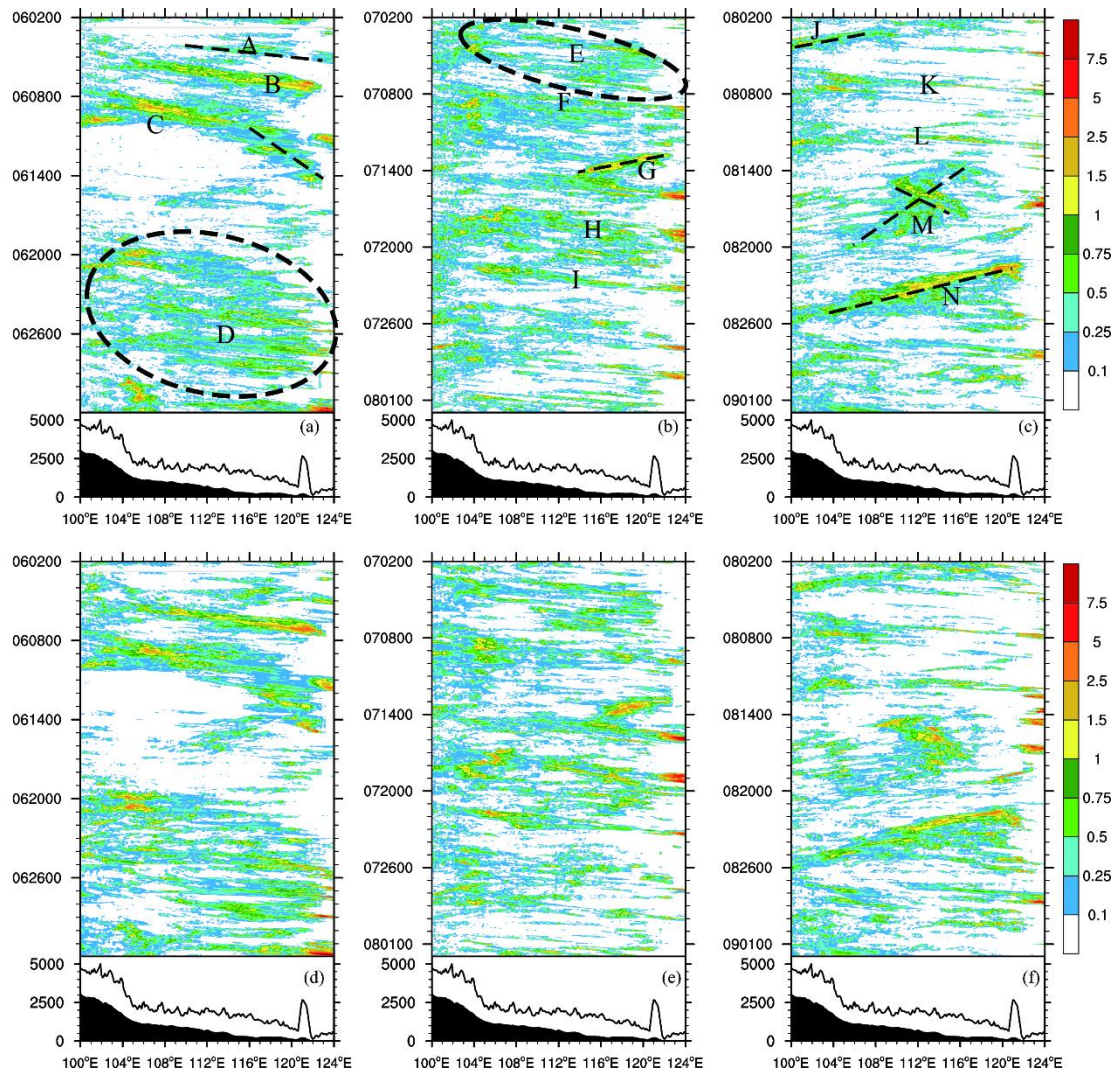
1092 Fig. 13. Local solar time (LST) corresponding to the peak diurnal precipitation in the (a)
 1093 observation and (b) WRF_NJU forecasts. The white ellipses and the black parallelogram
 1094 highlight regions where major differences exist between observations and forecasts.
 1095



1096
1097

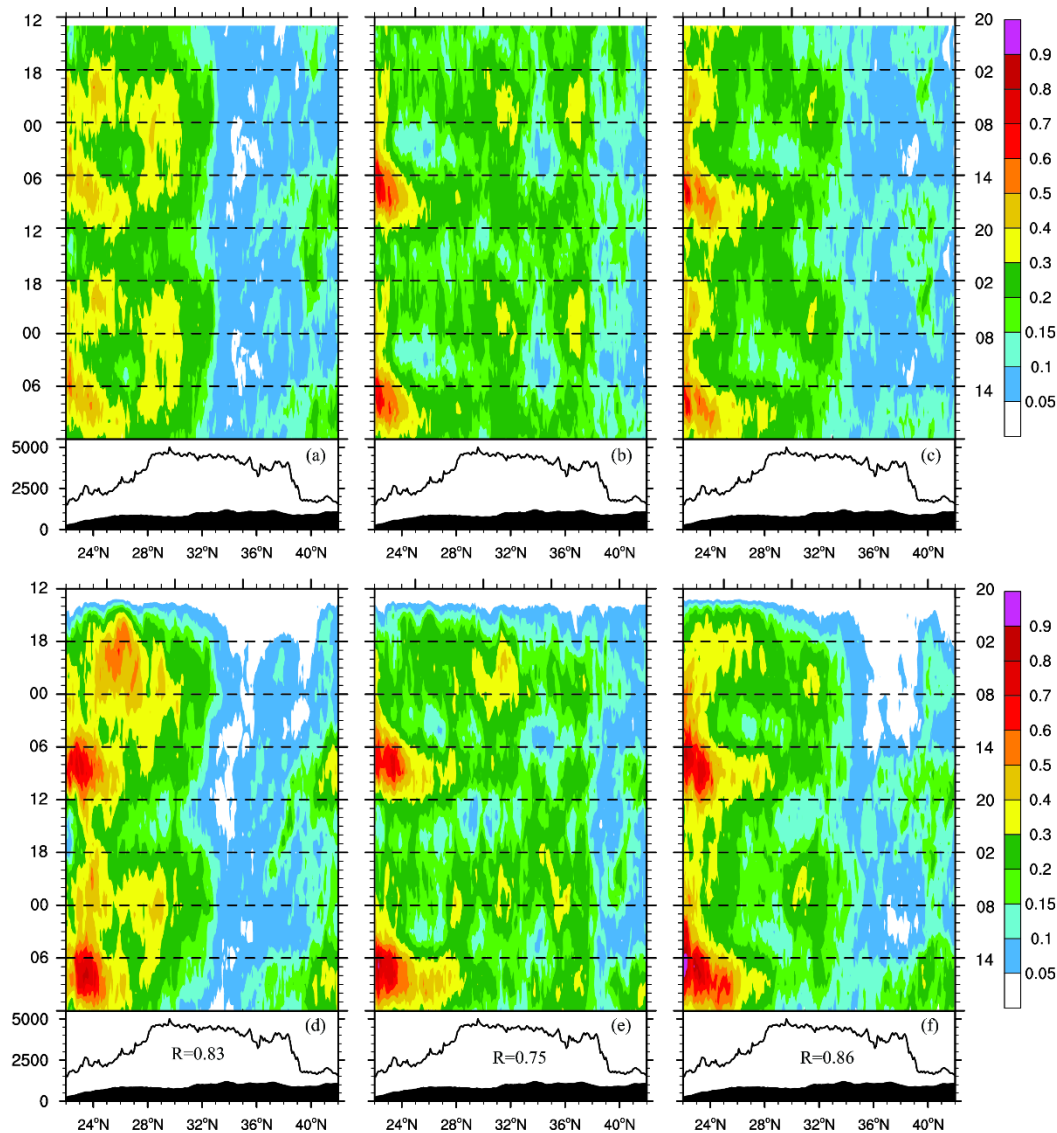
1098 Fig. 14. Time-latitude Hovmöller diagrams of rainfall in summer 2013. Rainfall is
1099 averaged from 100°E to 124°E within strips of 0.1° latitude width. The top and bottom
1100 rows represent rain gauge observations and WRF_NJU forecasts. The columns represent
1101 June, July and August. Curves and shadings below each subfigure show the maximum
1102 and mean terrain heights, respectively. Capital letters in the top row represent individual
1103 precipitation episodes.

1104



1105
1106
1107
1108

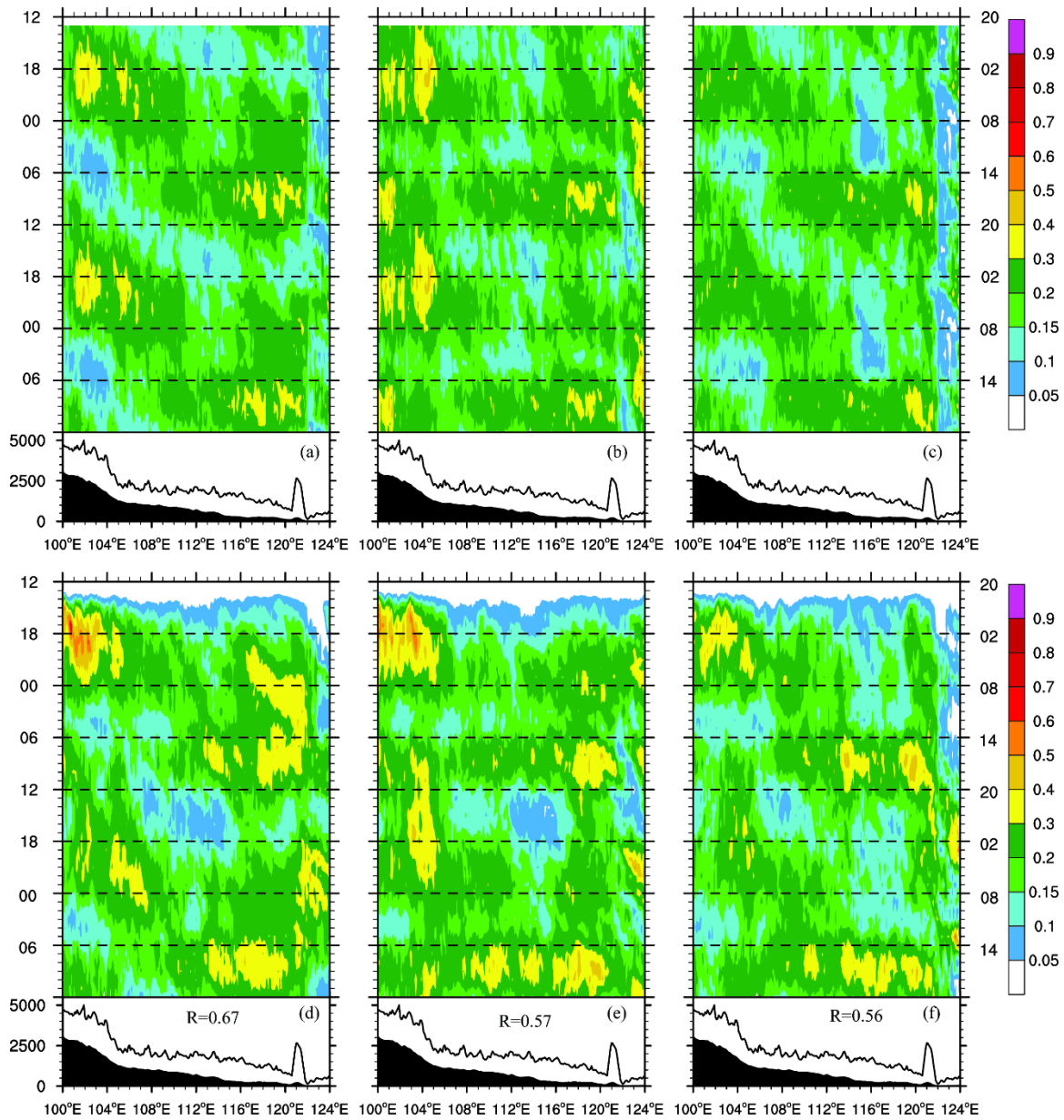
Fig. 15. As Fig. 12 but for the time-longitude Hovmöller diagrams. Rainfall is averaged from 22°N to 42°N within strips of 0.1° longitude width.



1109
1110

1111 Fig. 16. Hovmöller diagrams representing the diurnal cycle of precipitation averaged
1112 zonally within strips of 0.1° latitude width between 100°E and 124°E in years 2013-14.
1113 The top and bottom rows represent rain gauge observations and WRF_NJU forecasts.
1114 The columns represent June, July and August. The time-axes of left (right) are in UTC
1115 (LST). Data from all 48 hours of forecast starting at 12 UTC are included. The
1116 correlation coefficient (R) of the forecast with its corresponding observation is given in
1117 the bottom panels.

1118
1119



1120

1121

1122 Fig. 17. The same as Fig. 16 but for time-longitude diurnal cycle averaged meridionally
 1123 within strips of 0.1° longitude width between 22°N and 42°N .

1124